Defying Uncertainty: Reliable Barrier Coverage in Unstable Energy-Harvesting Networks

Pei Xu, *Member, IEEE*, Shi-Long Han, Chih-Yung Chang, *Member, IEEE*, and Diptendu Sinha Roy, *Senior Member, IEEE*

***Abstract*—Barrier coverage is essential in wireless sensor networks (WSNs) for detecting unauthorized intrusions across regions, but reliable surveillance is hindered by probabilistic boundary sensing under the probabilistic sensing model (PSM) and unstable solar energy in wireless rechargeable sensor networks (WRSNs). Adjustable sensing radii can reinforce weak regions but cause heterogeneous energy consumption, while many studies assume constant photovoltaic (PV) output. This article proposes energy-balanced cooperative sensing (EBCS), integrating MCTS-based PV scenario prediction, energy-balanced activation scheduling, grid-based cooperative detection, and island genetic algorithm (Island-GA) sensor selection to improve reliability, energy balance, and network lifetime. The representative numerical results show that the worst case barrier coverage quality $\bar{\Psi}^{\min}$ reaches 0.92 under high solar variability, with a DR-RMSE of 7.5% under abrupt PV shocks. The expected cooperative detection probability (ECPD) of EBCS remains high at 0.91–0.94 across varying sensor densities and adjustable sensing radii. Surveillance quality degradation (SQD) increases only slightly, indicating strong robustness. Grid resolution sensitivity shows path overlap ratio (POR) above 0.9 for w $\leq$ 6 m. CVaR-based control maintains energy-neutral operation (ENO) violation probability ρ below 5% in all seasons. These metrics directly demonstrate the framework's effectiveness and lead to the final summary. The key findings of the research include: efficient use of each sensor node's energy capacity, optimized initial energy allocation, enhanced load distribution across the network, improved energy fairness among nodes, and potential contribution to CO_2 emissions reduction through efficient solar utilization, reduced reliance on supplementary energy sources, and support for environmentally sustainable operation across all sensor clusters.**

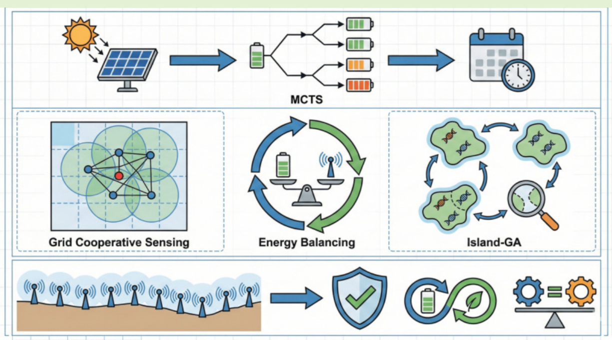

***Index Terms*—Adjustable sensing radius, barrier coverage, cooperative detection, energy harvesting (EH), energy-balanced scheduling, photovoltaic (PV) prediction, probabilistic sensing model (PSM), wireless sensor networks (WSNs).**

I. Introduction

WIRELESS sensor networks (WSNs) have been widely applied in seismic monitoring, environmental monitoring, and intrusion detection in hazardous areas [1], [2]. Among various research directions, coverage is one of the core topics and can be classified into target coverage, area coverage, and barrier coverage. Target coverage focuses on monitoring specific objects [3], such as museums or campuses; area coverage aims to monitor a designated region [4], such as farmland or chemical plants. In contrast to these two categories, barrier coverage seeks to detect intruders attempting to cross critical boundaries and is an essential mechanism for preventing unauthorized access [5].

Although studies on barrier coverage have made significant progress, two key challenges remain. First, due to the inherent limitations of sensing range and detection accuracy, the reliability of detection decreases significantly when intruders adopt stealthy paths or move near the sensing boundary. Second, sensors are powered by batteries, and both sensing and communication continuously consume energy, making it difficult to maintain stable long-term operation. Therefore, how to enhance monitoring reliability while prolonging network lifetime has become a central research objective [6], [7]. This

Received 22 May 2026; revised 10 June 2026; accepted 17 June 2026. Date of publication 29 June 2026; date of current version 3 August 2026. This work was supported in part by the Program for Key Scientific Research Projects in Colleges and Universities of Anhui Province under Grant 2022AH051781, in part by the Program for Scientific Research Fund for Talents in Hefei University under Grant 21-22RC16, and in part by the industry-sponsored research projects under Grant 902/22050124126 and Grant 902/22050124063. The associate editor coordinating the review of this article and approving it for publication was Dr. Muhammed Enes Bayrakdar. *(Corresponding author: Chih-Yung Chang.)*

Pei Xu and Shi-Long Han are with the School of Artificial Intelligence and Big Data, Hefei University, Hefei 230601, China (e-mail: xupei@hfuu.edu.cn; 18856698650@163.com).

Chih-Yung Chang is with the Department of Computer Science and Information Engineering, Tamkang University, New Taipei 25137, Taiwan (e-mail: cychang@mail.tku.edu.tw).

Diptendu Sinha Roy is with the Department of Computer Science and Engineering, National Institute of Technology, Shillong 793003, India (e-mail: diptendu.sr@nitm.ac.in).

Digital Object Identifier 10.1109/JSEN.2026.3706080

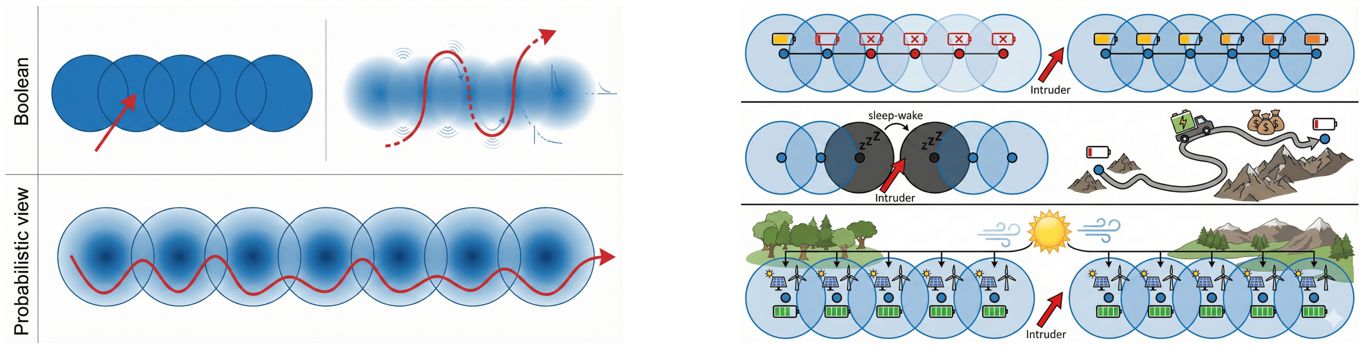

(a) (b)

Fig. 1. Some problems in previous studies. (a) First issue. (b) Second issue.

issue becomes even more severe in real-world scenarios where frequent battery replacement is infeasible.

Regarding the first challenge, the quality of barrier surveillance is influenced by both the sensing model and construction algorithms. As illustrated in Fig. 1(a), many existing studies [8], [22] construct k-barrier coverage using the Boolean sensing model (BSM), which assumes perfect detection within a fixed sensing radius. However, BSM fails to capture the effects of signal attenuation and noise in practical environments. When an intruder moves along a stealthy path or stays near the sensing boundary, its signal characteristics become weakened, resulting in a significantly decreased detection probability. In contrast, the probabilistic sensing model (PSM) [9] describes sensing capability using detection probability, thereby better reflecting uncertainty in boundary regions. Nonetheless, many related studies still assume sensors with fixed sensing radii [9], [10], [11], limiting adaptability to different intrusion trajectories.

With the increasing adoption of adjustable sensing radius sensors [12], [13], [14], boundary detection performance can be enhanced to some extent. However, this also introduces more complex scheduling and energy allocation challenges, as different sensing radii correspond to different energy consumptions. The limited computational capability of WSN nodes further hinders the direct use of advanced optimization techniques such as multiobjective optimization [27]. Similarly, advanced perception models, such as neuromorphic event-camera recognition with transfer-learning-enhanced multitask detection [28], further illustrate the computational burden of modern sensing intelligence and are difficult to directly deploy on energy-constrained WSN nodes.

The second major challenge is network lifetime. As shown in Fig. 1(b), since sensors operate on limited battery power and both sensing and communication continuously consume energy, maintaining long-term stable operation is difficult. Existing research mainly relies on sleep–wake mechanisms [15], [23] or energy-efficient algorithms [16], [17] to extend network lifetime, though their performance remains restricted by finite battery capacity. To alleviate this issue, wireless rechargeable sensor networks (WRSNs) have been introduced, and two main energy replenishment strategies have been proposed: mobile chargers [18], [19] and environmental energy harvesting (EH) [14], [20]. Although mobile chargers can deliver stable energy, the large-scale and complex terrain of typical barrier coverage scenarios make their deployment extremely expensive. In comparison, environmental EH is more suitable for such applications. Other WSN/WRSN studies have addressed channel-based back-off control in delay-constrained industrial WSNs [25], mobile data gathering with vehicle movement costs and capacity constraints [26], metaheuristic WSN deployment [31], and charging-based mechanisms for surveillance quality, connectivity, perpetual lifetime, and path reduction [32], [33]. These works improve communication, deployment, data collection, or charging efficiency, but they do not simultaneously consider PV fluctuation, adjustable-radius energy heterogeneity, and probabilistic cooperative barrier detection.

Solar EH has recently become a widely discussed topic across various countries. Compared with conventional energy sources, such as petroleum or coal, solar energy is more energy-efficient and environmentally friendly. However, solar energy availability varies greatly under different geographic and weather conditions, leading to significant instability. Most existing energy-harvesting-based studies [9], [10], [11], [15], [16], [17], [23] assume constant photovoltaic (PV) output and often overlook the effects of weather fluctuations. In reality, PV output varies over time, and this assumption may lead to conservative and coarse estimations, ultimately limiting the performance of WRSNs. Recent efforts have attempted to improve renewable-energy prediction and validation by combining historical and forecast weather data for wind and PV generation [21] and by designing automated CNN-LSTM architectures for solar irradiance forecasting [30]. However, these forecasting studies mainly focus on prediction accuracy itself and do not jointly translate day-ahead PV uncertainty into energy-neutral barrier-coverage scheduling under adjustable sensing radii.

Global renewable-energy deployment has grown rapidly in recent years, with solar, wind, hydropower, geothermal, and bioenergy sources increasingly integrated worldwide [34]. By the end of 2025, solar PV systems, wind energy, and bioenergy capacity continued to expand, accompanied by growing cumulative energy storage installations [35]. This surge in renewable-energy infrastructure highlights the shift toward sustainable and decentralized energy solutions. Such developments motivate the integration of solar-powered WRSNs, which can leverage locally harvested energy to provide reliable, long-term barrier monitoring while aligning with the global trend of renewable-energy adoption. Consequently, our study focuses on designing energy-efficient and high-reliability

WRSNs that are capable of sustainable operation under variable solar availability.

In summary, under the context of adjustable sensing radii and solar-powered operation, the research on barrier coverage must address the following three issues.

1) Solar energy fluctuates significantly with time, weather, and geographic conditions. Under such an uncertain energy supply, how can scheduling strategies guarantee stable and reliable operation?
2) Sensors exhibit distinct energy consumption levels under different sensing radii. To satisfy detection requirements while allocating energy efficiently, how should energy usage be planned across nodes?
3) Under the PSM, cooperative detection effectiveness varies across combinations of sensors. How can each node's contribution in cooperative sensing be quantified and utilized to enhance overall monitoring performance while enabling long-term operation?

To address the above challenges and improve the quality of barrier surveillance while maintaining energy neutrality, this article proposes a novel barrier coverage algorithm for WRSNs: the **energy-balanced cooperative sensing (EBCS)** algorithm.

To address the above challenges in a unified manner, the proposed EBCS algorithm integrates three key ideas: 1) next-day PV energy forecasting under uncertainty; 2) energy balancing under adjustable sensing radii; and 3) cooperative detection enhancement under the PSM. Multiple simulation experiments comparing the proposed method with previous studies [1], [5], [6], [7], [8], [9], [22] verify its effectiveness.

In summary, the main contributions of the proposed EBCS algorithm are as follows.

1) Introducing a predictable solar energy supply model to improve the accuracy of energy availability estimation. To address the difficulty of predicting solar energy under fluctuating weather and time conditions, this study is the first to apply Monte Carlo tree search (MCTS) to PV energy modeling. By inferring future energy distributions from historically similar scenarios, the predicted solar availability becomes more realistic, offering reliable energy support for subsequent scheduling.
2) Proposing an energy-balancing mechanism based on periodic scheduling to achieve efficient energy planning under adjustable sensing radii. To tackle the significant energy differences associated with different sensing radii, we design a periodic scheduling mechanism with time-slot division and balanced energy allocation. Sensors dynamically adjust activation duration according to predicted energy and their sensing radii, ensuring energy neutrality, preventing overload, and effectively prolonging network lifetime.
3) Constructing a grid-based cooperative sensing model to quantify and enhance multisensor joint detection capability. To address the difficulty of evaluating cooperative sensing performance under the PSM, we develop spatiotemporal detection units formed by equal-area grids and time slots, simplifying cooperative detection probability computation. Furthermore, by employing the island genetic algorithm (Island-GA) to select the most contributive neighboring sensors, overall monitoring quality is significantly enhanced.
4) Comprehensively validating the superiority of EBCS in monitoring quality and energy sustainability. Through extensive simulations, the proposed EBCS algorithm is compared with existing works [9], [10], [11], [15], [16], [17], [23], demonstrating notable improvements in energy utilization efficiency, cooperative detection performance, and barrier monitoring quality, highlighting the potential of EBCS in practical WRSN barrier coverage scenarios.

The proposed EBCS framework addresses critical challenges in WRSNs, including probabilistic boundary sensing and fluctuating PV energy availability. This work is important because it provides a method to maintain reliable barrier coverage while ensuring long-term energy-neutral operation (ENO) at each sensor node. The novelty of the study lies in combining MCTS-based PV scenario prediction, energy-balanced scheduling with adjustable sensing radii, grid-based cooperative sensing, and Island-GA sensor selection. Unlike previous approaches, the framework quantifies the contribution of weak paths, optimizes load distribution, and adapts dynamically to energy variations, resulting in improved coverage and energy fairness. Systematic experiments demonstrate that EBCS outperforms existing methods across various sensor densities and environmental conditions, highlighting both its practical significance and technical innovation.

The remainder of this article is organized as follows. Section II summarizes related work. Section III formalizes the assumptions and problem definitions. Section IV presents the EBCS algorithm. Section V provides performance evaluations. Section VI concludes this article and discusses future work.

II. Related Work

Early studies on WSNs typically treated sensor nodes as homogeneous units with fixed sensing radii. In recent years, research attention has gradually shifted toward integrating adjustable sensing range (ASR) with EH technologies to achieve finer-grained energy-efficiency management.

For the lifetime maximization problem in adjustable-range sensor networks (WSN-RAS), Chen et al. [1] proposed the neighborhood-based estimation of distribution algorithm (NEDA). Unlike traditional genetic algorithms, NEDA adopts an estimation of distribution algorithm (EDA) to explore the solution space and embeds a linear programming (LP) model directly into the evolutionary loop. The LP solver evaluates the contribution of each coverage configuration—namely, the activation duration—to the network lifetime, thereby aligning the search direction with global optimization. They further introduced a neighborhood sampling strategy (NSS) to avoid premature convergence and designed a heuristic repair strategy (HRS) based on residual energy to resolve potential coverage holes created during random solution generation. In the domain of target coverage, Sah et al. [9] introduced the ESTC algorithm, which leverages geometric analysis and set-covering theory. A target coverage graph (TCG) is constructed to identify critical targets, and a nondisjoint set strategy is employed. By interleaving the activation of different sets, ESTC enables nodes to participate in multiple sets under energy constraints, thereby significantly improving utilization efficiency.

Recent renewable-energy studies have broadened the design space of sustainable power systems and provided useful References for energy-aware networked applications. For remote and application-specific PV deployment, Alkhazmi et al. [36] analyzed PV solar street lighting systems in remote areas, while El-Khozondar and El-Batta [45] investigated solar energy adoption as an alternative to conventional energy in the Gaza Strip. For grid-supporting hybrid renewable-energy systems, Nassar et al. [37] examined hybrid solutions for mitigating power shortages in public electricity grids, and El-Khozondar et al. [40] conducted a technical–economic–environmental assessment of grid-connected hybrid renewable-energy systems. Ahmed et al. [41] further studied the optimal design of a PV/Wind/PHS hybrid system under multiple grid-connection constraints. In microgrid and smart-grid contexts, Khaleel et al. [38] improved microgrid performance through hybrid energy storage integration using ANFIS and GA approaches, while smart-grid technologies for sustainable urban development were discussed in [39]. AI-driven energy forecasting for smart grids has also been explored in [42], and hydrogen-based subgrid energy support has been investigated in [43]. For critical-service scenarios, El-Khozondar et al. [44] designed a standalone hybrid PV/wind/diesel-electric generator system for a COVID-19 quarantine center. Building on these renewable-energy developments, the integration of environmental EH has enabled classical BSMs to be progressively replaced by probabilistic models, better accommodating fluctuating energy availability in practical sensor networks.

Zhang et al. [5] developed the MSQBE algorithm for solar-powered networks, aiming to balance monitoring quality and energy consumption. Their prediction framework relies on historical weather similarity, and they introduced the concept of space–time bottleneck points. By dynamically adjusting slot lengths while strictly adhering to the ENO principle, MSQBE maximizes the joint detection probability at bottleneck regions. Building on deep learning (DL), Xu et al. [6] proposed the BCRAS algorithm for barrier coverage. Their CNN-LSTM hybrid model captures the spatiotemporal patterns of PV power, and cooperative sensing capability under the probabilistic model is quantified to schedule nodes with the largest marginal detection contribution to weak grids.

Beyond coverage control, energy optimization at the communication layer has gained substantial attention. Sarang et al. [7] introduced the PADC-MAC protocol, adopting a nonlinear autoregressive neural network (NARNET) to predict solar harvesting rates. The protocol employs an aggressive adaptive strategy: when abundant energy is predicted, the receiver increases its duty cycle to 100% to reduce latency, and receiver-initiated broadcasts mitigate idle listening at transmitters. At a broader level, Abdel-Basset et al. [8] and Kathole et al. [22] have demonstrated the potential of DL for complex spatiotemporal forecasting. In particular, Kathole et al. [22] developed SEP-CVSGCNN-IoT, which integrates complex-valued spatiotemporal graph convolution with the nutcracker optimization (NCO) algorithm, significantly enhancing predictive accuracy in dynamic environments.

However, despite the substantial progress in mathematical modeling and algorithmic innovation, two fundamental challenges regarding physical robustness and long-term sustainability remain unresolved.

First, idealized sensing models cause edge-detection failures and enable concealed path exploitation. NEDA [1] and ESTC [9] rely heavily on Boolean sensing assumptions, ignoring the decay of signal-to-noise ratio with distance. Optimization algorithms consequently push internode spacing toward the sensing limit, placing targets in persistent "low-SNR traps," where actual detection rates fall far below theoretical predictions. Even probabilistic approaches such as MSQBE [5] and BCRAS [6] focus primarily on static grid probabilities and fail to account for dynamic intruder behavior. A strategic adversary may compute a concealed path along detection "valleys," maintaining low trigger probability at all times and effectively bypassing the network. Moreover, dynamically reducing sensing radius for energy conservation sacrifices long-range robustness and creates artificial dynamic blind spots.

Second, excessive dependence on energy prediction and the computational overhead of "intelligent" models introduce a sustainability paradox. Aggressive scheduling strategies, such as those in PADC-MAC [7], rely critically on prediction accuracy; yet microclimate fluctuations (e.g., localized cloud shading) often exceed the representational capacity of historical data, leading to battery overdraft and cascading failures. Compounding this issue, executing computation-intensive models such as SEP-CVSGCNN [22] or CNN-LSTM [6] on resource-constrained IoT nodes results in substantial energy overhead, often outweighing the communication savings they aim to achieve. Finally, existing ENO models typically neglect battery aging and leakage currents, making long-term scheduling strategies vulnerable when deployed in real-world environments.

III. Assumption and Problem Statement

This section first introduces the network assumptions and system model of the WRSNs under consideration. It then outlines the formulation of the problem, including its objectives and the associated constraints.

A. Network Environment

We focus on a rectangular monitoring region R with dimensions $L \times W$, where L and W denote the length and width of R, respectively. The four boundaries of R are denoted by B_{left}, B_{right}, B_{top}, and B_{bottom}. For any point $v \in R$, its coordinates are written as (x_v, y_v). A set of solar-powered sensors $\mathcal{S} = \{s_1, s_2, \ldots, s_n\}$ is randomly deployed within R. Each sensor has an identical sensing radius that is adjustable among several discrete levels. Increasing the sensing radius of a sensor leads to both higher power consumption and stronger detection capability. Every sensor is assigned a unique ID and

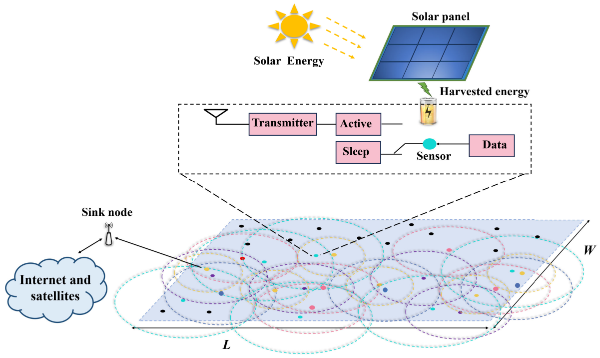

Fig. 2. Scenario of the considered WRSNs.

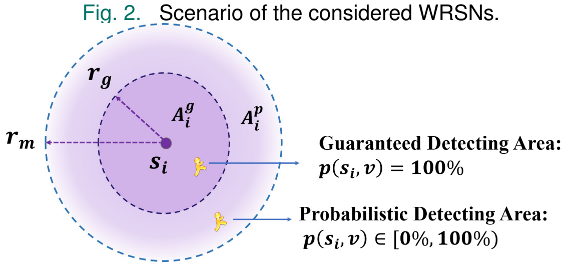

Fig. 3. Logical view of the PSM.

is assumed to be aware of its own location, residual energy, and the boundaries of R. The coordinates of sensor s_i are denoted by (x_i, y_i). The communication radius of each sensor is assumed to be at least twice the maximum sensing radius. The overall network scenario is illustrated in Fig. 2.

B. Probabilistic Sensing Model

The PSM is adopted in this study. In general, a sensor is more likely to detect an intruder when the target is closer. The conceptual structure of the PSM is illustrated in Fig. 3. Let $\mathbb{R} = \{r_1, r_2, \ldots, r_m\}$ be the set of selectable sensing radii, where $r_i < r_j$ for $i < j$. As shown in Fig. 3, the sensing range of sensor s_i consists of two parts: an inner guaranteed region $A_{s_i}^g$ with radius r_g, and an outer probabilistic region $A_{s_i}^p$ extending to r_m. An intruder located inside $A_{s_i}^g$ is detected with probability 1, while within $A_{s_i}^p$, the detection probability decreases monotonically with distance.

Let v_{loc} be the intruder location, and let $d(s_i, v_{\text{loc}})$ be the Euclidean distance between s_i and the intruder. The detection probability $p(s_i, v_{\text{loc}})$ follows:

$$p(s_i, v_{\text{loc}}) = \begin{cases} 1, & d(s_i, v_{\text{loc}}) \le r_g \\ e^{-\lambda\alpha^\gamma}, & r_g < d(s_i, v_{\text{loc}}) \le r_m \\ 0, & d(s_i, v_{\text{loc}}) > r_m \end{cases} \tag{1}$$

where $\alpha = d(s_i, v_{\text{loc}}) - r_g$, and λ and γ are the path-loss parameters characterizing sensing-signal attenuation.

In the PSM, the parameters λ and γ characterize the sensing attenuation behavior and are inherently environment-dependent. Specifically, the path-loss exponent γ reflects how rapidly the sensing probability decays with distance and typically varies across different environments (e.g., open areas, urban regions, or obstructed terrains), while the coefficient λ controls the overall attenuation strength under a given sensing range configuration. Although the same PSM formulation is adopted by EBCS and all baseline methods for fair comparison, different scheduling strategies may exhibit distinct sensitivities to variations in (λ, γ). Therefore, the robustness and generalizability of the proposed framework under diverse sensing environments warrant explicit evaluation, which is investigated through dedicated sensitivity experiments in Section V.

Path loss directly affects the sensing and communication efficiency of the studied WRSNs. Increased attenuation raises the energy cost of maintaining reliable operations [29], leaving less energy for sensing tasks and degrading monitoring quality. Since the PSM employed in the proposed EBCS algorithm is governed by (1), parameters λ and γ critically influence effective sensing capability under different environmental conditions. Section V evaluates the impact of path loss on the performance of the proposed EBCS algorithm through simulation experiments.

C. Charging and Discharging Stage

In the considered WRSNs, every sensor node is powered by solar energy. During the daytime, a sensor can operate in one of two modes: the *sensing–recharging* state, in which it simultaneously senses and harvests energy, or the *recharging-only* state, where it merely stores energy without performing sensing. At night, solar energy is unavailable, so each sensor can only be in either a *sensing-only* state or a *sleeping* state. We refer to a sensor as *active* whenever it is in the sensing–recharging or sensing-only state, since energy is consumed in both cases. In contrast, a sensor in the sleeping state neither executes tasks nor draws energy.

Let E be the battery capacity of each sensor. For sensor s_i, let $p_{i,x}^{\text{sen}}$ be the power consumption rate when it adopts sensing radius $r_x \in \mathbb{R}$. Following the model in [24], the sensing power of s_i is determined by its sensing radius and can be expressed as

$$p_{i,x}^{\text{sen}} = p_{i,m}^{\text{sen}} \left(\frac{r_x}{r_m}\right)^2 \tag{2}$$

where $p_{i,m}^{\text{sen}}$ is the given power consumption rate associated with the maximum sensing radius r_m.

In the proposed EBCS framework, the entire monitoring period is segmented into multiple cycles of identical duration. Each cycle is composed of uniform time slots, providing a structured basis to evaluate sensing performance in both space and time. Because a sensor consumes the most energy when using the maximum sensing radius r_m, we presume that the available energy in one cycle allows the sensor to remain active at radius r_m for only a single slot. This slot, with length τ, is treated as the fundamental unit for scheduling operations throughout each cycle.

For analytical convenience, we impose the following relationship between any sensing radius r_x and the maximal radius r_m:

$$\frac{r_m}{r_x} = \sqrt{m - x + 1}. \tag{3}$$

Combining (2) and (3), the total active time of sensor s_i within one cycle when it uses sensing radius r_x, denoted by $t_{i,x}^{\text{sen}}$, is given by

$$t_{i,x}^{\text{sen}} = (m - x + 1)\,\tau. \tag{4}$$

To enable tractable scheduling while preserving physical consistency, the continuous sensing-radius domain is discretized into a finite set of radius–time operating modes. Since sensing power grows quadratically with the sensing radius, a key concern is whether such discretization introduces heuristic distortions in energy accounting. The following theorem establishes that the adopted radius–time discretization is strictly energy-equivalent to the continuous quadratic sensing power model and further characterizes its refinement behavior as the number of discrete levels increases.

Theorem 1: (Energy-Equivalent Discretization and Asymptotic Refinement).

Setup: Consider the adjustable sensing radii set $R = \{r_1, r_2, \ldots, r_m\}$ with the maximum radius r_m. Under the quadratic sensing power model in (2), the discretized radius relationship in (3), and the slot-based active time assignment in (4), the following properties hold.

1) *Energy-Equivalence:* For any sensor s_i and any discrete sensing level $r_x \in R$, the total sensing energy consumed by operating at radius r_x for $t_{i,x}^{\text{sen}}$ is identical to that consumed by operating at the maximum radius r_m for one base slot τ, namely,

$$p_{i,x}^{\text{sen}} t_{i,x}^{\text{sen}} = p_{i,m}^{\text{sen}} \tau. \tag{5}$$

Therefore, the discretized relationship in (3) and (4) is energy-equivalent and fully consistent with the quadratic sensing power law in (2), rather than an ad hoc heuristic.

2) *Asymptotic Refinement in the Normalized Power Domain:* Define the normalized sensing-power ratio

$$\eta_x := \frac{p_{i,x}^{\text{sen}}}{p_{i,m}^{\text{sen}}} = \left(\frac{r_x}{r_m}\right)^2. \tag{6}$$

Under (6), the discrete set $\{\eta_x\}_{x=1}^{m}$ equals $\{1, 1/2, \ldots, 1/m\}$ up to ordering, and

$$\max_{x\in\{1,\ldots,m-1\}} \left|\eta_{x+1} - \eta_x\right| \le \frac{1}{m}. \tag{7}$$

Proof:

1) *Energy-Equivalence:* From (3), it follows that:

$$\frac{r_x}{r_m} = \frac{1}{\sqrt{m-x+1}}. \tag{8}$$

Substituting this relation into (2) yields

$$p_{i,x}^{\text{sen}} = p_{i,m}^{\text{sen}} \left(\frac{1}{\sqrt{m-x+1}}\right)^2 = \frac{p_{i,m}^{\text{sen}}}{m-x+1}. \tag{9}$$

Multiplying both sides by $t_{i,x}^{\text{sen}} = (m-x+1)\tau$ in (4), we obtain□

$$p_{i,x}^{\text{sen}} t_{i,x}^{\text{sen}} = \frac{p_{i,m}^{\text{sen}}}{m-x+1} \cdot (m-x+1)\,\tau = p_{i,m}^{\text{sen}} \tau. \tag{10}$$

2) *Asymptotic Refinement:* By the definition of η_x and the above derivation

$$\eta_x = \frac{p_{i,x}^{\text{sen}}}{p_{i,m}^{\text{sen}}} = \left(\frac{r_x}{r_m}\right)^2 = \frac{1}{m-x+1}. \tag{11}$$

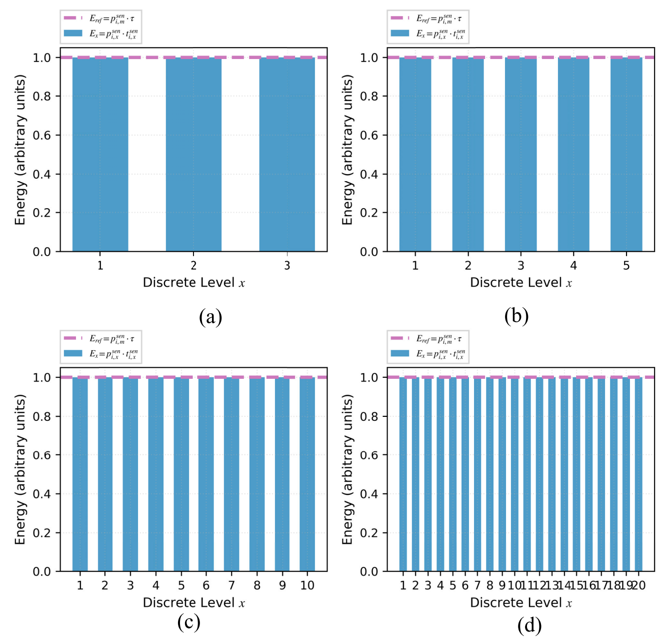

Fig. 4. Experimental verification of the energy-equivalence property in the proof of Theorem 1. (a) $m = 3$ levels (error: 2.22e-16). (b) $m = 5$ levels (error: 3.33e-16). (c) $m = 10$ levels (error: 3.33e-16). (d) $m = 20$ levels (error: 3.33e-16).

The maximum spacing between adjacent values in $\{1/k\}_{k=1}^{m}$ is

$$\max_{1\le k\le m-1} \left|\frac{1}{k} - \frac{1}{k+1}\right| = \max_{1\le k\le m-1} \frac{1}{k\,(k+1)} = \frac{1}{m\,(m-1)} \le \frac{1}{m}. \tag{12}$$

For any $\eta \in [1/m, 1]$, choosing $k = \lceil 1/\eta \rceil \in \{1, \ldots, m\}$ yields $|\eta - 1/k| \le 1/m$, let $\eta_x = 1/k$, since $k = \lceil 1/\eta \rceil$, it follows that:

$$\frac{1}{k} \le \eta < \frac{1}{k-1} \tag{13}$$

with the convention that $1/(k-1) = 1$ when $k = 1$. Hence,

$$0 \le \eta - \frac{1}{k} < \frac{1}{k-1} - \frac{1}{k} = \frac{1}{k\,(k-1)}. \tag{14}$$

Because $k \in \{1, \ldots, m\}$, we have

$$\frac{1}{k\,(k-1)} \le \frac{1}{m\,(m-1)} \le \frac{1}{m}. \tag{15}$$

Therefore,

$$|\eta - \eta_x| = \left|\eta - \frac{1}{k}\right| \le \frac{1}{m}. \tag{16}$$

This completes the proof. □

Figs. 4 and 5present numerical experiments that validate the two analytical properties established in Theorem 1. Fig. 4 focuses on verifying the energy-equivalence property of the discretized sensing model, while Fig. 5 evaluates the refinement and approximation behavior of the discretized normalized sensing-power ratios as the number of discrete radius levels increases.

Fig. 4 shows the verification of energy equivalence under different discretization resolutions $m = 3, 5, 10$, and 20. For each discrete level x, the total sensing energy consumption is computed as $E_x = p_{i,x}^{\text{sen}} t_{i,x}^{\text{sen}}$ and compared with the reference

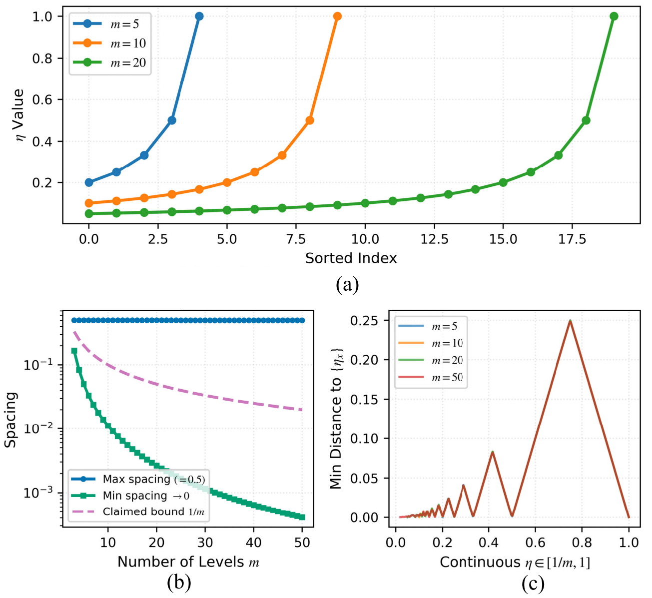

Fig. 5. Experimental analysis of the asymptotic refinement property in the proof of Theorem 1. (a) Distribution of. (b) Space versus m (critical analysis). (c) Approximation quality.

energy $E_{\mathrm{ref}} = p_{i,m}^{\mathrm{sen}}\tau$. As observed, the energy values at all discrete levels coincide with the reference energy up to machine-level numerical errors, confirming that the discretized radius–time construction in (3) and (4) is strictly energy-equivalent to the continuous quadratic sensing power model. This result indicates that operating at a lower sensing radius for a proportionally longer duration consumes the same total energy as operating at the maximum radius for one base time slot.

Fig. 5 examines the refinement behavior of the discretized normalized sensing-power ratios η_x. Fig. 5(a) illustrates the distribution of $\{\eta_x\}$ over $[1/m, 1]$, revealing a nonuniform structure with denser sampling in the low-power region and coarser spacing near full power. Fig. 5(b) and (c) quantifies the approximation behavior induced by this discretization. While the global maximum spacing between adjacent discrete levels is dominated by the interval $[1/2, 1]$ and remains unchanged as m increases, the minimum spacing decreases rapidly, indicating progressive refinement in the low-power regime. The oscillatory error pattern in Fig. 5(c) arises from nearest-neighbor projection onto a discrete set and shows that approximation errors decrease substantially in the low-power region as m increases.

Overall, the results in Figs. 4 and 5demonstrate that the proposed discretization preserves exact energy equivalence across discrete sensing levels and provides a controllable and physically interpretable approximation of the continuous sensing-power domain.

An illustrative example of this model is depicted in Fig. 6. In this example, the set of available sensing radii is $\mathbb{R} = \{r_1, r_2, \ldots, r_m\}$. According to (3), we obtain

$$r_x = \frac{r_m}{\sqrt{m-x+1}}, \quad r_1 = \frac{r_m}{\sqrt{m}}. \tag{17}$$

As shown in Fig. 6, when sensor s_i operates at the maximum radius r_m, it can be active for only one time slot in each

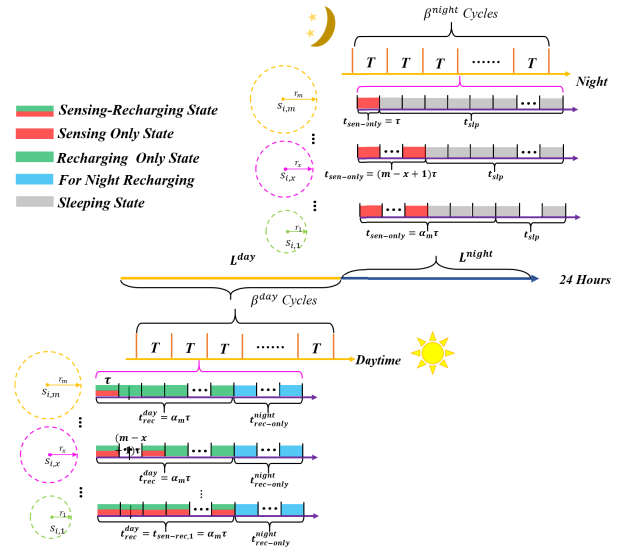

Fig. 6. Example of charging and discharging model.

cycle. If s_i selects an intermediate radius r_x, its active duration increases to $(m - x + 1)\tau$, and when it chooses the smallest radius r_1, the active time reaches $m\tau$ within the same cycle.

D. Problem Statement

This study investigates the barrier coverage problem in WRSNs where each sensor can adjust its sensing radius. The proposed EBCS scheme develops a distributed scheduling method that assigns an appropriate working plan to every sensor with the goal of improving monitoring performance while ensuring long-term energy sustainability. The formulation of the objective and related constraints is given below.

Let s be a feasible scheduling strategy, and let DB_s be the barrier generated under strategy s. For the hth slot t_h within cycle T_c, define $S_{v,h}^{act}(s)$ as the set of sensors active at slot t_h under strategy s that can cover point v. For any space–time coordinate (v, h) with $v \in R$ and $t_h \in T_c$, the cooperative detection probability contributed by these sensors is denoted by $p_{v,h}^s$ and computed as

$$p_{v,h}^s = 1 - \prod_{s_i \in S_{v,h}^{act}(s)} (1 - p(s_i, v)). \tag{18}$$

Let $\mathbb{C}$ be the set of all potential crossing paths, and let c_j be the jth path. The monitoring capability of DB_s on path c_j at slot t_h is defined as

$$q_h(s, j) = \max_{v \in c_j} p_{v,h}^s. \tag{19}$$

To evaluate the weakest temporal performance of the barrier, we define the surveillance quality on path c_j over the whole cycle as

$$q(s, j) = \min_{t_h \in T_c} q_h(s, j). \tag{20}$$

The overall surveillance performance of DB_s is then measured by the path with the lowest quality

$$q(s) = \min_{c_j \in \mathbb{C}} q(s, j). \tag{21}$$

Since both the number of paths and the number of points on each path can be infinite, a grid-based discretization method is applied, and the details are given in Section IV.

To render the continuous barrier coverage problem tractable, the grid side length w determines the resolution of candidate grid cells and thus the granularity at which cooperative detection potentials are evaluated. Smaller values of w preserve fine-grained spatial variations and enable a more faithful characterization of localized weak regions, whereas coarse grids merge heterogeneous areas into single cells, potentially smoothing out local minima and shifting the geometric location of the identified weakest path.

From an optimization perspective, weakest-path identification relies on relative comparisons of cooperative detection potentials across adjacent columns. Accordingly, the choice of w affects both the feasible path set on the discretized domain and the numerical bottleneck values used to rank candidate paths. While coarser discretization reduces computational burden by shrinking the candidate set, it may gradually degrade geometric fidelity and coverage optimality due to approximation errors. This motivates the sensitivity study in Section V, which quantitatively examines how discretization granularity influences weakest-path consistency and the associated reliability–efficiency tradeoff.

Consistent with common practices in renewable-energy and energy-system optimization studies [43], [46], the proposed EBCS scheduling problem is explicitly organized as an optimization problem with a clearly defined decision strategy, objective function, and constraints. The decision variable is the feasible scheduling strategy s, which determines the working state and sensing-radius configuration of each sensor over the considered slots. Based on the cooperative detection quality defined in (18)–(21), the objective function of EBCS is to maximize the minimum surveillance quality over all potential crossing paths and time slots, where the subscript s in (22) explicitly identifies the scheduling strategy as the optimization variable

$$\max_{s} \; q(s). \tag{22}$$

The objective function in (22) is optimized subject to the following operational and energy-neutrality constraints. These constraints ensure that each sensor occupies a valid working state, participates in sensing within each cycle, and balances its scheduled sensing consumption with the harvested solar energy. Specifically, the state-exclusiveness constraint applies to every sensor and every time slot, the sensing-participation constraint applies to every sensor in each cycle, and the energy-related constraints apply to every sensor.

First, to characterize the per-slot operation of each sensor, we introduce the binary state variables $M_{j,h}^{\text{sen-cha}}$, $M_{j,h}^{\text{sen-only}}$, $M_{j,h}^{\text{cha-only}}$, and $M_{j,h}^{\text{sle}}$, which indicate whether sensor s_j is performing sensing–charging, sensing-only, charging-only, or sleeping at slot t_h, respectively. Since these variables are binary indicators, each sensor must occupy exactly one state in any slot, leading to the state-exclusiveness constraint for every sensor s_j and every time slot t_h

$$M_{j,h}^{sen\text{-}cha} + M_{j,h}^{sen\text{-}only} + M_{j,h}^{cha\text{-}only} + M_{j,h}^{sle} = 1. \tag{23}$$

Second, to avoid inactive or unused nodes in the constructed barrier, each sensor is required to participate in sensing at least once in each cycle, which gives the sensing-participation constraint for every sensor s_j in every cycle

$$\sum_{h=1}^{T_c/\tau} \left(M_{j,h}^{sen\text{-}cha} + M_{j,h}^{sen\text{-}only} \right) \geq 1 \quad \forall s_j. \tag{24}$$

Third, for every sensor s_i, the energy-related constraints are formulated according to the predicted solar supply and the radius-dependent sensing consumption. Let $p_i^{PV}(t)$ be the solar power generation of sensor s_i at time t. The harvestable daytime energy is

$$\int_{t_s}^{t_e} p_i^{PV}(t)\, dt. \tag{25}$$

The corresponding daily sensing energy consumption of each sensor s_i under the adopted scheduling strategy is expressed as

$$\sum_{j=1}^{T/T_c} \left(p_{i,x}^{sen} \cdot t_{i,x}^{sen} \right) \tag{26}$$

where T is the duration of a full day.

Finally, to maintain sustainable operation under the principle of ENO, the harvested energy and scheduled sensing consumption of each sensor s_i are balanced through the following energy-neutrality constraint:

$$\int_{t_s}^{t_e} p_i^{PV}(t)\, dt = \sum_{j=1}^{T/T_c} \left(p_{i,x}^{sen} \cdot t_{i,x}^{sen} \right). \tag{27}$$

Thus, the optimization problem in (22) is solved under the operational constraints in (23) and (24) and the energy-neutrality constraint in (25)–(27). Constraint (23) is enforced for each sensor and each time slot, constraint (24) is enforced for each sensor in each cycle, and constraints (25)–(27) are enforced for each sensor, jointly ensuring feasible sensor-state scheduling, periodic sensing participation, and sustainable energy usage over repeated cycles.

The PV energy model used by the proposed EBCS scheduling framework is provided in the Appendix II-A. For completeness, the Appendix II-B also summarizes a standard wind-harvesting reference model as supplementary context for possible PV/wind hybrid energy-harvesting extensions; however, wind generation is not included in the optimization constraints, scheduling process, or simulation results of this article.

E. Energy Fairness and Its Long-Term Implications

In addition to maximizing the weakest-path surveillance quality, a practical barrier should avoid systematic energy deprivation on a subset of nodes. Otherwise, even if the barrier quality is high in the short term, those overused sensors may experience frequent energy outages and become unavailable, which in turn undermines long-term barrier reliability. To formalize this notion, we define the per-cycle energy dynamics and an energy-fairness criterion.

Consider cycle k (with duration T_c) and sensor s_i. Let $E_i(k)$ be its stored energy at the beginning of cycle k, and let $H_i(k)$

and $C_i(k)$ be, respectively, the harvested and consumed energy within cycle k under strategy s. The energy evolution is

$$E_i(k+1) = \Pi_{[0,E_{\max}]}(E_i(k) + H_i(k) - C_i(k)) \tag{28}$$

where $\Pi_{[0,E_{\max}]}(x) = \min\{E_{\max}, \max\{0, x\}\}$ clips the battery level into $[0, E_{\max}]$. Define the per-cycle energy balance as

$$\Delta_i(k) = H_i(k) - C_i(k) \tag{29}$$

and its normalized version

$$\delta_i(k) = \frac{\Delta_i(k)}{H_i(k) + \varepsilon} \tag{30}$$

with a small $\varepsilon > 0$ to avoid division by zero.

Definition 1 (Energy Fairness): Given a horizon of K cycles, we say a scheduling strategy s is energy-fair if it keeps the energy-balance dispersion among nodes bounded, e.g.,

$$\mathrm{Var}(\delta_1(k), \ldots, \delta_N(k)) \le \xi \quad \forall k = 1, \ldots, K \tag{31}$$

for some small constant $\xi \ge 0$, or equivalently if it maximizes the Jain fairness index

$$J_\delta(k) = \frac{\left(\sum_{i=1}^{N} \delta_i(k)\right)^2}{N \sum_{i=1}^{N} \delta_i^2(k)} \in (0, 1] \tag{32}$$

where larger $J_\delta(k)$ indicates better fairness.

Definition 2 (Node Survivability): Sensor s_i is said to be survivable over K cycles if its stored energy never depletes, i.e., $E_i(k) > 0$ for all $k = 1, \ldots, K$.

Theorem 2: (Fair Energy Balance Implies Long-Term Survivability).

Setup: Assume that for each sensor s_i and each cycle k, the energy balance satisfies

$$\Delta_i(k) \ge -\eta \tag{33}$$

for some $\eta \ge 0$. If the initial energy satisfies $E_i(1) > \eta$, then $E_i(k) > 0$ holds for all $k = 1, \ldots, K$; hence s_i is survivable over the horizon.

Proof: From (28)–(33), we have

$$E_i(k+1) \ge \max\{0, E_i(k) - \eta\}.$$

By induction, $E_i(k) \ge E_i(1) - (k-1)\eta$ before clipping at zero. Since $E_i(1) > \eta$, we obtain $E_i(2) > 0$, and repeating the argument yields $E_i(k) > 0$ for all $k \le K$ as long as the per-cycle deficit is bounded by η.□

This theorem clarifies the long-term implication: enforcing bounded and uniform deficits (high energy fairness) prevents a small set of sensors from repeatedly suffering large negative balances, thereby reducing premature energy outages and improving barrier persistency.

The above formulation is established under an ideal slotted execution assumption, where sensors switch their working states exactly at slot boundaries and scheduling commands are delivered reliably. In practical WRSN deployments, such ideal conditions may be violated due to clock offsets, switching delays, and occasional packet loss. As a result, the sensing actions executed within a slot may deviate from the planned schedule or be applied with a short temporal misalignment. These nonideal execution effects do not change the problem objective or the long-term energy sustainability constraints imposed by (23)–(27), but they may perturb the realized cooperative sensing performance and the achieved barrier surveillance quality. The robustness of the proposed framework under imperfect synchronization and unreliable command delivery is quantitatively evaluated in Section V.

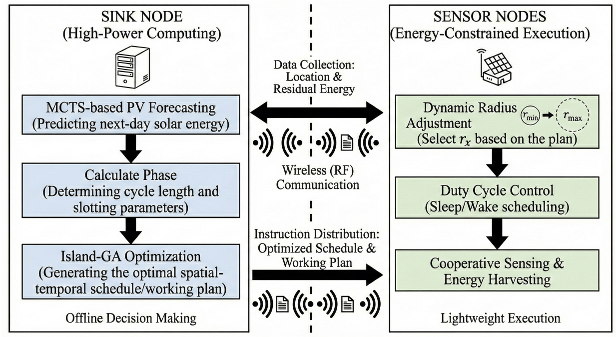

Fig. 7. Sink-assisted hierarchical (semi-centralized) execution architecture and information exchange of the proposed framework.

Section IV presents the proposed EBCS algorithm designed to satisfy constraints (23)–(27) while optimizing (22).

IV. Proposed EBCS Framework

This section presents the designed EBCS framework, which is divided into three main components: first, PV forecasting based on a Monte Carlo tree; second, the calculation phase; and finally, constructing the best schedule for each sensor using a GA algorithm. The proposed framework adopts a hierarchical (semi-centralized) execution architecture, in which computationally intensive components—including the MCTS-based day-ahead PV forecasting and the Island-GA-based scheduling optimization—are executed at sink nodes rather than at individual sensor nodes. Each sink node manages a local cluster of sensors within its communication range and is assumed to have substantially stronger energy supply, computation, and storage capability than ordinary sensor nodes, while sensor nodes only perform lightweight sensing operations and execute scheduling commands disseminated by the sink. This design is fundamentally different from fully centralized or fully distributed implementations and significantly improves the practical deployability of the proposed framework. Each component is detailed in the following subsections.

To further clarify the deployment architecture and information exchange, Fig. 7 illustrates the execution flow of the proposed framework. Specifically, the MCTS-based day-ahead PV forecasting, the DP-based decision modules (e.g., grid selection/bottleneck-related evaluations), and the Island-GA-based schedule optimization are executed at the sink node (or equivalently, a sink/cluster-head with high-power computing capability) in a clusterwise manner. These computations are performed at two time scales: at day-start, the sink runs the MCTS procedure to obtain the day-ahead PV profile and determine the cycle/slot parameters; at cycle-start, the sink performs the required DP-based evaluations and the Island-GA optimization to generate the per-sensor working plan. During network operation, sensor nodes only report lightweight runtime states (e.g., location and residual energy) via RF communication and execute the received scheduling commands, including duty-cycle control and dynamic sensing-radius adjustment. This sink-assisted hierarchical execution minimizes computation and coordination overhead on energy-constrained sensors while maintaining scalability through parallel operation across multiple sink-managed clusters.

The proposed framework adopts a hierarchical semi-centralized execution architecture, where computation-intensive modules (including MCTS-based day-ahead PV forecasting and GA-based schedule construction) are executed at the sink node, while sensor nodes only report lightweight runtime states and locally enforce the received duty-cycle commands. Under this architecture, frequent intraday rescheduling would introduce substantial communication overhead and nonnegligible dissemination delay, which can make the updated schedule stale when microclimate conditions evolve quickly. In contrast, the MCTS predictor builds a scenario tree at day-start to explicitly cover diverse PV realizations, so a single fixed day-ahead schedule can implicitly account for intraday uncertainties without repeated network-wide reoptimization. Therefore, fixing the schedule over the day is a deliberate system-level design choice that balances robustness, timeliness, and overhead.

A. Monte Carlo Tree Search

At day-start, our pipeline must fix the cycle and slot lengths from a full next-day PV power profile so that the daytime integral of the PV curve (available solar energy) can be balanced against per-sensor consumption. Unlike prior studies that predominantly employ end-to-end DL for PV forecasting, we replace fixed-window DL predictors with a scenario-tree approach searched by MCTS, using terrain-aware priors to produce day-ahead predictions from meteorological inputs (irradiance, temperature, humidity, and cloud cover). Under a rollout budget $\mathcal{N}$ with progressive widening, the online cost scales as $O(\mathcal{N}H) + O(\mathcal{N}^{1+\alpha})$; for the target H and accuracy regime, this is lower and more controllable than one-shot forward of representative deep models (see Theorem 3). Fixed-window predictors restrict each time step's decision to a length-L context and yield a single deterministic mapping at inference, whereas the MCTS-searched tree admits variable-length temporal context and conditions on the full day-ahead covariate path, providing strictly higher selectivity (see Theorem 4).

We first construct the scenario tree $\mathcal{T}$ offline from historical pairs $\mathcal{D} = \{(\boldsymbol{\xi}_t, P_t)\}_r$, where each meteorological vector is $\boldsymbol{\xi}_t =$ (irradiance, temperature, humidity, cloud cover). The database is organized into conditional candidate pools by month m, time-step index h, and terrain regime

$$terr \in \left\{\begin{array}{r} \text{desert}-\text{semiarid corridor} \\ \text{temperate inland plains} \\ \text{coastal}-\text{riverine corridor} \\ \text{highland corridor} \end{array}\right\}.$$

For each node identified by $(m, h, terr)$, a small set of PV snippets is generated via block-bootstrap conditional sampling; these sets form the node's admissible actions and act as priors for the subsequent search. To control branching, candidates are revealed gradually according to progressive widening, which will later limit expansion via (35).

At day-start, given the full forecast path $\boldsymbol{\Xi} = (\boldsymbol{\xi}_1, \ldots, \boldsymbol{\xi}_H)$ built from the same meteorological covariates, MCTS rolls forward on $\mathcal{T}$. Each node corresponds to time step h with context inferred from $\boldsymbol{\Xi}$ and stores a small action set $\mathcal{A}(n)$. Child selection follows:

$$\text{UCB}(n) = R(n) + c\sqrt{\frac{\ln N(\text{parent}(n))}{1 + N(n)}} \tag{34}$$

where $R(n)$ and $N(n)$ are the empirical mean return and visit count, respectively, and $c > 0$ trades off exploitation and exploration; expansion is gated by

$$|\mathcal{A}(n)| < c_{\text{pw}} [N(n)]^{\alpha}, \quad c_{\text{pw}} > 0,\ \alpha \in (0, 1) \tag{35}$$

so that new candidates are admitted only when sufficiently supported by visits. Choosing an action at time step h yields a PV sample P_h and advances the state to $h + 1$; a rollout completes to H, after which the path return is back-propagated to update R and N. Repeating this procedure $\mathcal{N}$ times produces full-day trajectories $\{\boldsymbol{P}^{(k)}\}_{k=1}^{\mathcal{N}}$, with $\boldsymbol{P}^{(k)} = (P_1^{(k)}, \ldots, P_H^{(k)})$.

During rollouts, each simulated day is scored by a risk–return objective that penalizes energy shortfall and curtailment and (optionally) rewards usable energy, thereby biasing the search toward energy-feasible, low-waste scenarios. Let E_{use} be the usable daily energy obtained by time-step–level battery-constrained accumulation (charging-rate limits, efficiencies, and capacity capping), E_{tar} a day-level energy target, $D = \max(0, E_{\text{tar}} - E_{\text{use}})$ the deficit, and W the total curtailed energy. Define

$$R = -\text{CVaR}_{\alpha}[D] - \lambda_{\text{waste}} W + \lambda_{\text{util}} \Phi(E_{\text{use}}) \tag{36}$$

$$D = \max(0, E_{\text{tar}} - E_{\text{use}}) \tag{37}$$

with CVaR_{α} measuring tail risk of shortfall and $\Phi(\cdot)$ a monotone utility (set $\lambda_{\text{util}} = 0$ when only robustness is desired).

Because subsequent phases require a single full-day curve fixed at day-start, the trajectory set is aggregated by a day-fixed quantile. Fix $\tau_0 \in (0, 1)$ (e.g., median $\tau_0 = 0.5$; conservative $\tau_0 = 0.25$; optimistic $\tau_0 = 0.9$) and define the time-stepwise prediction

$$\widehat{P}_h^{(\tau_0)}(\boldsymbol{\Xi}) = \text{Quantile}_{\tau_0}\left(\left\{P_h^{(k)}(\boldsymbol{\Xi})\right\}_{k=1}^{\mathcal{N}}\right), \quad h = 1, \ldots, H \tag{38}$$

which yields the full-day PV curve

$$\widehat{\boldsymbol{P}}^{(\tau_0)}(\boldsymbol{\Xi}) = \left(\widehat{P}_1^{(\tau_0)}(\boldsymbol{\Xi}), \ldots, \widehat{P}_H^{(\tau_0)}(\boldsymbol{\Xi})\right). \tag{39}$$

At day-start, a single quantile level τ_0 is fixed; the resulting full-day profile $\widehat{\boldsymbol{P}}^{(\tau_0)}$ is committed and remains unchanged throughout the day (no intraday reselection or branch switching). If a time-consistent single scenario is preferred over pointwise quantiles, one may select from $\{\boldsymbol{P}^{(k)}\}$ the trajectory minimizing $\sum_h w_h (P_h^{(k)} - \widehat{P}_h^{(\tau_0)})^2$ for nonnegative weights w_h. This formulation makes the data usage explicit: the scenario tree is trained from historical meteorological data—irradiance, temperature, humidity, and cloud cover—paired with historical

PV power; at day-start, the forecast of the same covariates drives conditional sampling, and MCTS search on $\mathcal{T}$, from which a single, time-consistent, day-ahead PV profile is produced.

Theorem 3 shows that the proposed MCTS-based PV prediction model achieves a lower online computational complexity than representative DL models [7], [8], [22] under a unified accuracy target and hardware baseline. The specific statement is given as follows.

Theorem 3: (Complexity Separation of MCTS Versus End-to-End DL Under a Unified Baseline; Time-Step Form).

Setup: A day has H time steps. At day-start, MCTS is run on a terrain-aware scenario tree with UCB and progressive widening that enforces (35). Each rollout incurs constant per-layer cost (selection, update, reward). Per-time-step battery accumulation is $O(1)$–$O(\log H)$. The output is a day-fixed quantile τ_0. For time step h, the true cdf is F_h. Near the τ_0-quantile $q_h(\tau_0)$, the density admits a positive lower bound $f_{\min} > 0$.

Deep-learning baselines are energy-net style energy-net neural network ensemble (ENNE), prediction-based adaptive duty cycle prediction-based adaptive MAC algorithm (PAMA), and complex-valued spatiotemporal graph convolutional neural network (CVSG). Their parameter counts are $p_{\mathrm{ENNE}}, p_{\mathrm{PAMA}}, p_{\mathrm{CVSG}}$. Let $p_{\min} = \min\{p_{\mathrm{ENNE}}, p_{\mathrm{PAMA}}, p_{\mathrm{CVSG}}\}$.

Claim: Fix confidence $\delta \in (0, 1$ and per-time-step quantile error $\varepsilon_q > 0$. If the DKW rollout budget and the margin condition below hold, then the day-start MCTS complexity is strictly smaller than the unified DL baseline.

Proof:

1) *MCTS Online Complexity Upper Bound:* Consider $\mathcal{N}$ rollouts and depth at most H. Path cost is $O(\mathcal{N}H)$. Under (35), expansion cost is $O(\mathcal{N}^{1+\alpha})$. Hence there exist constants $C_1, C_2 > 0$, such that

$$C_{\mathrm{MCTS}}(\mathcal{N}, H) \le C_1 \mathcal{N} H + C_2 \mathcal{N}^{1+\alpha}. \tag{40}$$

2) *Rollout Budget for Quantile Accuracy:* Fix time step h. Let $\widehat{F}_h$ be the empirical cdf of $\{P_h^{(k)}\}_{k=1}^{\mathcal{N}}$. By the Dvoretzky–Kiefer–Wolfowitz (DKW) inequality

$$\Pr\left(\sup_x \left|\widehat{F}_h(x) - F_h(x)\right| \le \varepsilon\right) \ge 1-\delta \quad \text{if} \quad \mathcal{N} \ge \frac{1}{2\varepsilon^2} \ln \frac{2}{\delta}. \tag{41}$$

If F_h has density at least $f_{\min}$ near $q_h(\tau_0)$, inverse-cdf stability gives

$$\left|\widehat{q}_h(\tau_0) - q_h(\tau_0)\right| \le \frac{\varepsilon}{f_{\min}} + O\left(\varepsilon^2\right). \tag{42}$$

Choose $\varepsilon = \varepsilon_q f_{\min}$ and assume the local linear regime. Then,

$$\mathcal{N} \ge \frac{f_{\min}^2}{2\varepsilon_q^2} \ln \frac{2}{\delta}. \tag{43}$$

Substituting (40) into (43) and absorbing constants into $K_1, K_2 > 0$ yields the high-probability bound

$$C_{\mathrm{MCTS}} \le K_1 H \frac{f_{\min}^2}{\varepsilon_q^2} \ln \frac{2}{\delta} + K_2 \left(\frac{f_{\min}^2}{\varepsilon_q^2} \ln \frac{2}{\delta}\right)^{1+\alpha}. \tag{44}$$

3) *Unified Lower Bound for One-Shot DL Forward:* For any end-to-end network N_j with p_j parameters on the same platform, a full-day forward requires at least a constant times p_j elementary operations. Hence, for some $c_{\mathrm{fw}} > 0$

$$C_{\mathrm{DL},j} \ge c_{\mathrm{fw}} p_j, \quad j \in \{\mathrm{ENNE}, \mathrm{PAMA}, \mathrm{CVSG}\} \tag{45}$$

and, therefore,

$$\min_j C_{\mathrm{DL},j} \ge c_{\mathrm{fw}} p_{\min}. \tag{46}$$

4) *Margin Condition and Separation:* Assume there exists $\kappa \in (0, 1)$ such that

$$K_1 H \frac{f_{\min}^2}{\varepsilon_q^2} \ln \frac{2}{\delta} + K_2 \left(\frac{f_{\min}^2}{\varepsilon_q^2} \ln \frac{2}{\delta}\right)^{1+\alpha} \le \kappa\, c_{\mathrm{fw}} p_{\min}. \tag{47}$$

Combining (44) and (47) gives

$$C_{\mathrm{MCTS}} \le \min_j C_{\mathrm{DL},j}. \tag{48}$$

□ □

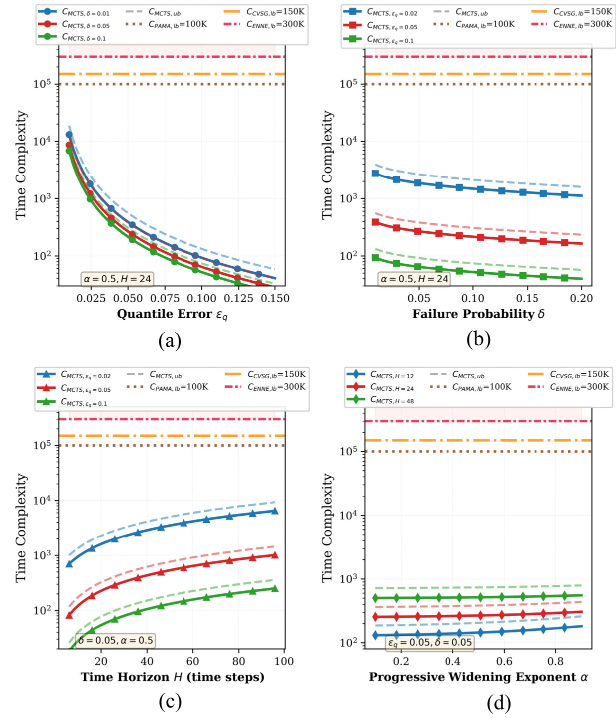

Fig. 8. Experiment of the proof of Theorem 3. (a) Impact of precision ε_q. (b) Impact of confidence $(1 - \delta)$. (c) Impact of time horizon H. (d) Impact of expansion exponent α.

Fig. 8 consists of four subplots that jointly illustrate the complexity separation predicted by Theorem 3 between the proposed MCTS-based predictor and the three DL baselines ENNE, PAMA, and CVSG. In Fig. 8(a), *impact of precision* ε_q, we vary the target quantile error ε_q while fixing $\delta = 0.05$, $\alpha = 0.5$, and $H = 24$. The solid curves $C_{\mathrm{MCTS},\delta}$ show that the MCTS time complexity decreases rapidly as ε_q becomes larger, and they closely track the theoretical upper bounds $C_{\mathrm{MCTS,ub}}$ (dashed curves in the same colors), whereas the three DL models remain at their constant lower-bound levels $C_{\mathrm{PAMA,lb}} = 10^5$, $C_{\mathrm{CVSG,lb}} = 1.5 \times 10^5$, and $C_{\mathrm{ENNE,lb}} = 3 \times 10^5$. Fig. 8(b), *impact of confidence* $(1 - \delta)$, sweeps the failure probability δ for several fixed values of ε_q. As δ increases from 0.02 to 0.2, the MCTS complexity curves decrease only mildly, reflecting the weak logarithmic dependence on $\ln(2/\delta)$

in (44), and they consistently stay more than one order of magnitude below all three DL baselines.

Fig. 8(c), *impact of time horizon* H, plots the MCTS complexity and its bound as the horizon length grows from 10 to 100 time steps with $\varepsilon_q = 0.05$, $\delta = 0.05$, and $\alpha = 0.5$. The solid curves $C_{\mathrm{MCTS},\varepsilon_q}$ increase roughly linearly in H, in agreement with the $O(H)$ term in (40), but even at $H = 100$ they remain far below the horizontal complexity levels of ENNE, PAMA, and CVSG, which validates the margin condition in (47). Finally, Fig. 8(d), *impact of expansion exponent* α, examines how the progressive-widening exponent influences complexity for three representative horizons $H \in \{12, 24, 48\}$ under $\varepsilon_q = 0.05$ and $\delta = 0.05$. The MCTS curves exhibit only a gentle growth with α, and across all α and H values, the corresponding C_{MCTS} and $C_{\mathrm{MCTS,ub}}$ remain at least two orders of magnitude smaller than the lower bounds of the three DL models. Overall, the four subplots in Fig. 8 provide a consistent visual confirmation of Theorem 3, demonstrating that the proposed MCTS-based PV prediction model enjoys a substantial computational complexity advantage over the three competing deep-learning models under a wide range of accuracy and algorithmic parameters.

Following the computational-complexity result in Theorem 3, Theorem 4 further clarifies the representational advantage of the proposed MCTS-based PV prediction model. Its main content is that, under the same discretized covariate space and action sets, the proposed MCTS predictor has strictly higher selectivity than fixed-window DL predictors [7], [8], [22]. For fixed-window DL models, the prediction at each time step is constrained by a bounded historical window. Thus, even when the input covariates and action sets are identical, the model can only distinguish a limited number of local temporal contexts. In contrast, the MCTS scenario-tree predictor can condition its decisions on variable-length historical prefixes and the full day-ahead meteorological path. This enables the search process to distinguish a richer set of possible PV evolution scenarios and to select more diverse energy-feasible day-ahead trajectories. Therefore, Theorem 4 complements Theorem 3: while Theorem 3 establishes the computational advantage of MCTS, Theorem 4 explains its higher selectivity and stronger scenario-representation capability. To keep the main algorithmic presentation concise, the formal statement, proof, and supporting selectivity experiments of Theorem 4 are presented in the Appendix I.

Theorem 4: (Bounded Gain of Intraday Replanning Under System Overhead; Day-Ahead Commitment Form).

Setup: Let $P(t)$ be the realized PV power trajectory over a day. At day-start, a full-day forecast $\hat{P}^0(t)$ is produced by the MCTS-based predictor, based on which a full-day sensing schedule is computed and committed. Consider an intraday replanning policy that performs K updates during the same day; after the kth update, the refined forecast is denoted by $\hat{P}^k(t)$. Let $Q(\hat{P})$ be the optimal barrier surveillance quality achieved when the schedule is optimized under the assumed PV profile $\hat{P}(t)$ with ENO constraints enforced. Assume that $Q(\cdot)$ is Lipschitz continuous with respect to the L_1 distance between PV profiles, i.e., there exists a constant $L_Q > 0$ such that for any two profiles $\hat{P}^a(t)$ and $\hat{P}^b(t)$

$$\left|Q\left(\hat{P}^a\right) - Q\left(\hat{P}^b\right)\right| \le L_Q \int \left|\hat{P}^a(t) - \hat{P}^b(t)\right| \mathrm{d}t. \tag{49}$$

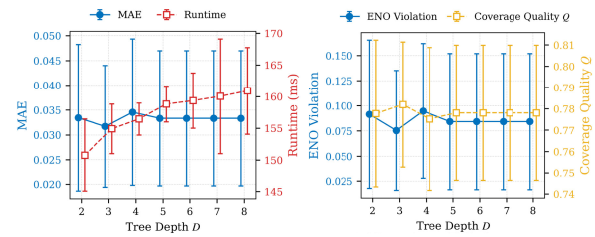

(a) (b)

Fig. 9. Sensitivity of the bounded-gain property to MCTS tree depth. (a) Prediction accuracy and computational cost versus tree depth. (b) Downstream ENO violation and surveillance quality versus tree depth.

For the rolling update sequence, define the remaining prediction error after the kth update as

$$\varepsilon_k \triangleq \int_{H_k} \left|P(t) - \hat{P}^k(t)\right| \mathrm{d}t \tag{50}$$

where H_k denotes the remaining time horizon after the kth update (hence ε_k is nonincreasing in k).

Claim: The total improvement in achievable surveillance quality obtained by K rounds of intraday replanning is upper bounded by

$$\Delta_K \le L_Q \sum_{k=1}^{K} (\varepsilon_{k-1} - \varepsilon_k) \le L_Q \varepsilon_0. \tag{51}$$

Moreover, if each replanning round incurs a nonnegligible system overhead due to communication and computation, then the cumulative overhead increases at least linearly with K, implying that frequent intraday replanning is not cost-effective when ε_0 is sufficiently small or the per-round overhead is nontrivial.

Proof: By the adopted ENO model, intraday replanning cannot introduce additional harvested energy; its sole effect is to reduce the mismatch between the assumed PV profile and the realized one over the remaining horizon. By (49), the maximum improvement in achievable surveillance quality attributable to the kth replanning step is bounded by $L_Q(\varepsilon_{k-1} - \varepsilon_k)$. Summing over $k = 1, \ldots, K$ yields the first inequality in (51). Since $\{\varepsilon_k\}$ is nonincreasing, the telescoping sum satisfies $\sum_{k=1}^{K}(\varepsilon_{k-1} - \varepsilon_k) \le \varepsilon_0$, which gives the second inequality in (51).

On the other hand, each replanning round necessarily requires at least one information exchange (to collect updated energy states and cooperative coverage summaries) and one schedule recomputation. Therefore, the cumulative system overhead grows at least linearly with the number of replanning rounds K. When this overhead outweighs the bounded gain in (51), further intraday replanning becomes inefficient. This completes the proof. □

To empirically substantiate the bounded-gain property established in Theorem 5 and to illustrate its practical implications under realistic system overhead, we conduct a set of controlled sensitivity experiments by varying the key hyperparameters of the MCTS-based day-ahead predictor, namely the tree depth

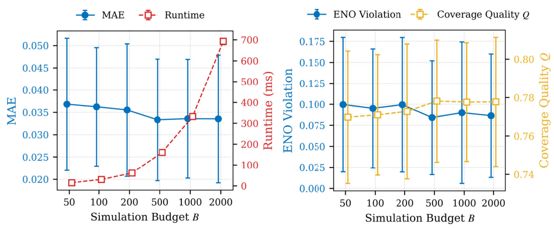

Fig. 10. Sensitivity of the bounded-gain property to MCTS simulation budget. (a) Prediction accuracy and computational cost versus simulation budget. (b) Downstream ENO violation and surveillance quality versus simulation budget.

D and the simulation budget B. The corresponding results are summarized in Figs. 9 and 10.

Fig. 9(a) and (b) examines the effect of increasing the tree depth D on the prediction accuracy and the downstream system performance. As D increases, the MAE of the day-ahead PV forecast quickly stabilizes, and both the ENO violation probability and the achieved coverage quality remain essentially unchanged beyond moderate depths. This observation empirically supports the Lipschitz-type regularity assumption on $Q(\cdot)$ adopted in Theorem 5, as further refinements of the forecast yield diminishing reductions in the remaining prediction error ε_k, and hence only marginal improvements in the achievable surveillance quality.

Meanwhile, Fig. 9(a) shows that the runtime grows monotonically with D, reflecting the increased computational burden of deeper MCTS trees. This contrast between the rapidly saturating performance gain and the steadily increasing overhead directly mirrors the bounded-gain inequality in (51), indicating that aggressive replanning based on deeper trees is not cost-effective once the dominant forecast uncertainty has been resolved.

A consistent trend is observed when varying the simulation budget B, as shown in Fig. 10(a) and (b). Increasing B leads to a modest improvement in MAE at small budgets, but the gains quickly plateau, while the runtime exhibits a pronounced growth. Meanwhile, the ENO violation probability and the resulting coverage quality remain largely insensitive to further increases in B. These results empirically confirm that the cumulative improvement in surveillance quality attainable through additional replanning is effectively upper-bounded, whereas the associated system overhead continues to accumulate.

Taken together, these experimental results provide an empirical validation of Theorem 5 by demonstrating that, under a hierarchical semi-centralized execution architecture, the marginal benefit of intraday replanning rapidly diminishes once a reasonably accurate day-ahead forecast is available. This explains why committing to a single day-ahead schedule, as adopted in the proposed framework, is not only theoretically justified by the bounded-gain analysis but also practically preferable in the presence of nonnegligible computation and communication overhead.

B. Calculation Phase

After predicting the next day's PV power, the fit PV power function $p_i^{PV}(t)$ is obtained for day j. Since sensors harvest energy only during daytime, part of the acquired energy must support nighttime operation. The harvested energy is

$$E_{\text{cha}} = \int_{t_s}^{t_e} p_i^{PV}(t)\, dt. \tag{52}$$

Thus,

$$E_{day}^{sen} + E_{night}^{sen} = E_{\text{cha}}. \tag{53}$$

Under the charging–discharging model, one time slot of length τ supports one sensing action at maximum radius r_m

$$\tau = \frac{E_{day}^{sen}}{p_{i,m}^{sen}}. \tag{54}$$

Assume each cycle contains $\alpha + \beta$ slots. During daytime, α slots balance daytime energy consumption. The energy equilibrium is

$$\frac{\int_{t_s}^{t_e} p_i^{PV}(t)\, dt}{t_e - t_s}\, \alpha\tau = p_{i,m}^{sen}\tau. \tag{55}$$

Hence,

$$\alpha = \frac{p_{i,m}^{sen}(t_e - t_s)}{\int_{t_s}^{t_e} p_i^{PV}(t)\, dt}. \tag{56}$$

The cycle counts are

$$N_{day}^{c} = \frac{t_e - t_s}{(\alpha+\beta)\tau}, \qquad N_{night}^{c} = \frac{T - t_e + t_s}{(\alpha+\beta)\tau}. \tag{57}$$

Daytime and nighttime energy consumption are

$$E_{day}^{sen} = N_{day}^{c}\, p_{i,m}^{sen}\tau, \qquad E_{night}^{sen} = N_{night}^{c}\, p_{i,m}^{sen}\tau. \tag{58}$$

Balancing harvested and consumed energy yields

$$\left(N_{day}^{c} + N_{night}^{c}\right)\tau\, p_{i,m}^{sen} = \int_{t_s}^{t_e} p_i^{PV}(t)\, dt. \tag{59}$$

The parameter β follows from (56)–(59), and the resulting cycle length is

$$T_c = \frac{T\,\tau\, p_{i,m}^{sen}}{\int_{t_s}^{t_e} p_i^{PV}(t)\, dt}. \tag{60}$$

A sensor detects a grid $g_{(x,y)}$ only if the grid is fully covered. Otherwise, the detection probability is zero. Let $v_{i,(x,y)}^{\text{far}}$ be the farthest point in the grid from sensor s_i. Then,

$$p\left(s_i, g_{(x,y)}\right) = p\left(s_i, v_{i,(x,y)}^{\text{far}}\right). \tag{61}$$

If multiple sensors cover the grid, the cooperative detection probability is

$$p^{\text{co}}\left(\Phi_{(x,y)}, g_{(x,y)}\right) = 1 - \prod_{s_k \in \Phi_{(x,y)}} \left(1 - p\left(s_k, g_{(x,y)}\right)\right). \tag{62}$$

These probabilities are used to identify bottleneck grid–time points and to construct the sensor task schedule.

C. Constructing the Best Schedule and GA Algorithm

The first step is constructing the best schedule, which aims to estimate, in an energy-aware yet scheduling-agnostic manner, the cooperative detectability potential of each grid cell, and then select exactly one cell per column so that the selected cells form a continuous left-to-right chain. The chain is optimized lexicographically: first maximize the bottleneck (the minimum potential along the chain), and among ties maximize the chainwise sum. This yields the spatial backbone for building the best schedule for each sensor.

To clarify the overall schedule-construction procedure before introducing detailed formulations, we summarize the pipeline as follows. First, grid-level cooperative potentials and feasibility conditions are evaluated under energy constraints. Second, a dynamic-programming-based chain selection is performed to identify the optimal spatial backbone. Third, based on the selected chain, an Island-GA is employed to construct per-sensor duty-cycle and sensing-radius schedules while ensuring per-cycle energy neutrality. The final output is a feasible and optimized working plan for each sensor, which is then disseminated for execution.

To formalize the above procedure, we first define the grid representation and the adjacency relation used for chain construction. The monitored region is partitioned into a $c_1 \times c_2$ grid (rows $\times$ columns). Let $g(x, y)$ be the cell at row $x \in \{1, \ldots, c_1\}$ and column $y \in \{1, \ldots, c_2\}$. Right-hand adjacency is

$$\mathcal{N}_r\left(g\left(x, y\right)\right) = \left\{g\left(x', y+1\right) : \left|x' - x\right| \le 1\right\}. \tag{63}$$

Let $\Phi_r(x, y)$ be the set of sensors that fully cover $g(x, y)$ at sensing radius r. Admissible radii are either continuous in $[r_{\min}, r_{\max}]$ or taken from a discrete set $\mathcal{R}_d$. Perfect communications are assumed; single-sensor detection follows the model $p_{\text{det}}^{(k)}(r)$ (sensor k, radius r). From Step 2, slotting parameters are inherited: slot length τ, M slots per cycle, N_{cyc} cycles per day, and $T = N_{\text{cyc}} M$ daily slots.

For sensor k, let E_k^{harv} be the next-day harvestable-energy lower bound, E_k^{base} the baseline, and $e_k(\tilde{r})$ a nominal per-activation energy at a representative radius $\tilde{r}$. Define the availability duty cycle

$$\alpha_k = \min\left\{1,\ \frac{E_k^{\text{harv}} - E_k^{\text{base}}}{N_{\text{cyc}} M\, e_k\left(\tilde{r}\right)} + \epsilon\right\}, \qquad \epsilon > 0 \tag{64}$$

(preventing degenerate zero-division behavior).

At $r_{\max}$, define the energy-weighted coverage density

$$\rho_{\text{eff}}\left(x, y\right) = \sum_{k \in \Phi_{r_{\max}}(x,y)} \alpha_k \tag{65}$$

and its normalized version

$$\hat{\rho}_{\text{eff}}\left(x, y\right) = \frac{\rho_{\text{eff}}\left(x, y\right) - \rho_{\text{eff}}^{\min}}{\rho_{\text{eff}}^{\max} - \rho_{\text{eff}}^{\min}} \in [0, 1] \tag{66}$$

where $\rho_{\text{eff}}^{\min}$ and $\rho_{\text{eff}}^{\max}$ are the minimum and maximum values of $\rho_{\text{eff}}(x, y)$ over all cells.

The radius preference is, then,

$$r^{\star}\left(x, y\right) = r_{\min} + \left(r_{\max} - r_{\min}\right) \psi\left(\hat{\rho}_{\text{eff}}\left(x, y\right)\right) \tag{67}$$

where $\psi : [0, 1] \to [0, 1]$ is monotone nondecreasing (default $\psi(t) = t$; convex emphasis: $\psi(t) = t^{\gamma}$, $\gamma \ge 1$). If radii are discrete, project $r^{\star}(x, y)$ to the nearest level in $\mathcal{R}_d$.

If all sensors share the same energy model, $\alpha_k = \alpha$ becomes a constant and $\hat{\rho}_{\text{eff}}$ reduces to the normalized coverage count at $r_{\max}$.

Let

$$B_k = E_k^{\text{harv}} - E_k^{\text{base}} \tag{68}$$

be the next-day usable energy, and

$$\mathcal{R}_k^{(1)} = \left\{r : e_k\left(r\right) \le B_k\right\} \tag{69}$$

the set of radii affording at least one activation. Define the fairness radius

$$r_k^{\text{fair}} = \max \mathcal{R}_k^{(1)} \tag{70}$$

and the geometric coverage limit

$$r_k^{\text{cov}}\left(x, y\right) = \max\left\{r : k \text{ still fully covers } g(x, y) \text{ at radius } r\right\}. \tag{71}$$

Given $r^{\star}(x, y)$, define the individually feasible radius on $g(x, y)$ as

$$r_k^{\text{use}}\left(x, y\right) = \min\left\{r^{\star}\left(x, y\right),\ r_k^{\text{cov}}\left(x, y\right),\ r_k^{\text{fair}}\right\}. \tag{72}$$

Exclude sensors with $r_k^{\text{use}}(x, y) < r_{\min}$. The strict participant set is

$$\Phi_r\left(x, y\right) = \left\{k \in \Phi_{r_{\max}}\left(x, y\right) : r_k^{\text{use}}\left(x, y\right) \ge r_{\min}\right\}. \tag{73}$$

If $r^{\star}(x, y)$ is overly aggressive, use the feasible-participant ratio

$$\theta\left(x, y; r\right) = \frac{\left|\left\{k \in \Phi_r\left(x, y\right) : r_k^{\text{use}}\left(x, y\right) \ge r\right\}\right|}{\left|\Phi_r\left(x, y\right)\right|} \tag{74}$$

and back off to the largest admissible radius

$$r_k^{\text{feas}}\left(x, y\right) = \sup\left\{r \le r^{\star}\left(x, y\right) : \theta\left(x, y; r\right) \ge \theta_0\right\}$$
$$\theta_0 \in (0, 1]. \tag{75}$$

The participant set $\Phi(\tilde{x}, y)$ is then updated accordingly. Convert individual budgets to per-grid daily supply

$$C_k\left(x, y\right) = \left\lfloor \frac{B_k}{e_k\left(r_k^{\text{use}}\left(x, y\right)\right)} \right\rfloor \tag{76}$$

and define

$$\lambda\left(x, y\right) = \min\left\{1,\ \frac{\displaystyle\sum_{k \in \Phi(x,y)} C_k\left(x, y\right)}{T}\right\}. \tag{77}$$

Retain only cells satisfying the hard feasibility threshold

$$\lambda\left(x, y\right) \ge \lambda_0, \qquad \lambda_0 \in (0, 1] \text{ (typically } \lambda_0 = 1) \tag{78}$$

and discard the rest. Under the deployment assumption, each column contains at least one feasible cell.

In contrast, the communication cost remains low and stable when $|S|$, D, and L_{node} stay at moderate levels. These observations imply that practical deployments should prioritize reducing per-node message payloads and controlling network scale, as these two strategies provide the most substantial improvement in communication efficiency.

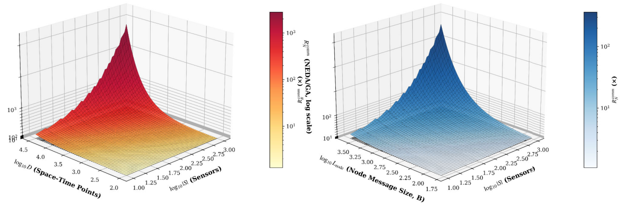

Fig. 11. Comparison of the communication consumption with the related works.

The second is the DP method. Define the cooperative potential of $G(x, y)$ under perfect communications as

$$W(x, y) = 1 - \prod_{k\in\Phi(x,y)} \left(1 - p_{\mathrm{det}}^{(k)}\left(r_k^{\mathrm{feas}}(x, y)\right)\right) \in [0, 1] \quad (79)$$

optionally computed in the log-domain for numerical stability.

Cast the one-cell-per-column chain selection as an algebraic path problem over a lexicographic semiring with carrier

$$S = [-\infty, 1] \times [-\infty, \infty) \quad (80)$$

and operations

$$(b_1, s_1) \oplus (b_2, s_2) = \max_{\mathrm{lex}} \{(b_1, s_1), (b_2, s_2)\} \quad (81)$$

$$(b_1, s_1) \otimes (b_2, s_2) = (\min\{b_1, b_2\},\ s_1 + s_2) \quad (82)$$

with neutral elements

$$\mathbf{0} = (-\infty, -\infty), \qquad \mathbf{1} = (1, 0) \quad (83)$$

and node weights

$$w(x, y) = (W(x, y),\ W(x, y)). \quad (84)$$

Dynamic programming on the layered DAG proceeds as follows. For column $y = 1$

$$g(x, 1) = w(x, 1) \quad (85)$$

and for $y \geq 2$

$$g(x, y) = w(x, y) \otimes \bigoplus_{g(x',y-1)\in\mathcal{N}_{y-1}^{-1}(g(x,y))} g\left(x', y-1\right) \quad (86)$$

where $\mathcal{N}_{y-1}^{-1}(g(x, y))$ denotes the set of left neighbors in column $y - 1$. The global optimum is

$$g^{\star} = \bigoplus_{x} g(x, c_2) = \left(\tau_{\mathrm{opt}}, s_{\mathrm{opt}}\right) \quad (87)$$

whose first component τ_{opt} is the optimal bottleneck and second component s_{opt} is the maximal sum among all bottleneck-optimal chains. A standard backtracking on stored predecessors yields the target chain $\{g_1^{\mathrm{tar}}, \ldots, g_{c_2}^{\mathrm{tar}}\}$.

Fig. 11 illustrates how the communication load ratio R_{comm}^{N} scales with the key system parameters. Both surfaces show a clear upward trend, with the steepest growth occurring in the upper-right regions, indicating that communication overhead increases super-linearly when the number of sensors grows together with either the space–time resolution D (left) or the node message size L_{node} (right). Among these factors, $|S|$ exerts the strongest influence, and the right plot further suggests that the system is more sensitive to message size than to spatiotemporal density.

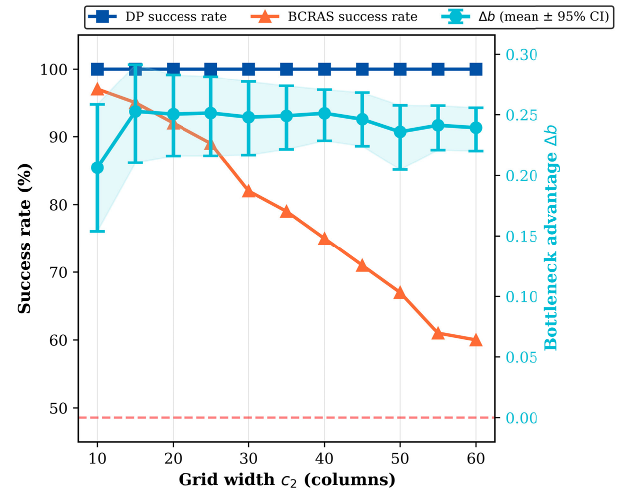

Fig. 12. Comparison of the performance of the proposed DP method with the baseline BCRAS across different grid widths.

Fig. 12 compares the performance of the proposed DP method with the baseline BCRAS across different grid widths c_2. The DP success rate remains consistently near 100% for all grid sizes, demonstrating strong robustness to spatial scaling. In contrast, BCRAS exhibits a clear monotonic decline as c_2 increases, with the success rate falling from above 95% at small grids to around 60% at $c_2 = 60$. This trend indicates that BCRAS becomes increasingly unstable in wider grids, whereas the DP method maintains reliable path selection.

The right axis shows the bottleneck advantage Δb (mean $\pm$ 95% CI), which stays positive across all tested widths, confirming that the DP-selected chains consistently achieve better bottleneck quality than BCRAS. Although Δb gradually increases with larger grids, the advantage remains statistically significant. Together, these results show that the DP method not only preserves high success rates but also provides consistently stronger bottleneck performance under increasing spatial complexity.

D. Assumptions, Limitations, and Uncertainties

To clarify the boundaries of our methodology and the scope of the results, we outline the underlying assumptions, potential limitations, and sources of uncertainties, consistent with previous studies on hybrid renewable-energy systems [47].

1) Assumptions: We assume that sensor nodes are deployed with known locations and adjustable sensing radii, and that solar energy availability can be reasonably estimated using day-ahead PV forecasting. Communication among sensors and sink nodes is assumed reliable, and environmental conditions are represented through the PSM.

2) Limitations: The proposed EBCS framework relies on the accuracy of day-ahead PV predictions and does not explicitly model long-term battery degradation, hardware failures, or extreme environmental shocks. The system performance is also dependent on the predefined time-slot discretization, which may limit temporal resolution.

3) Uncertainties: The effectiveness of the scheduling strategy may vary due to stochastic variations in solar energy, unpredictable microclimate events, and potential packet loss or sensor synchronization errors. The simulation results provide probabilistic performance evaluations under representative scenarios, but real-world deployments may experience deviations from modeled behavior.

E. Holistic Computational and Communication Overhead Analysis

This section provides a unified evaluation of the computational and communication overhead introduced by the proposed multistage optimization framework. Based on the execution flow in Section IV and Table I, the overhead is analyzed at the system level by jointly accounting for the complexity of each phase and the communication cost incurred during schedule dissemination and execution.

1) *Execution Structure:* The proposed framework adopts a sink-assisted hierarchical architecture. All computation-intensive procedures—including day-ahead PV prediction, cooperative detection evaluation, bottleneck space–time identification, and GA-based schedule construction—are executed at the sink node. Sensor nodes only perform slot-level state switching $M_{j,h}(\cdot)$ according to received scheduling commands. This separation enables a clear distinction between centralized optimization cost and distributed execution cost.

2) *Computational Overhead:*
The computational overhead consists of a one-time day-start optimization and repeated cycle-level computations. At the day-start, the MCTS-based PV prediction constructs the next-day energy profile. Each rollout expands at most H levels and is repeated N times, resulting in a computational complexity on the order of $\mathcal{O}(NH)$. Since this procedure is executed only once per day, its cost is amortized across all cycles.
During each cycle, the sink first evaluates cooperative detection probabilities over all sensor–grid pairs, which incurs a complexity of $\mathcal{O}(|S||G|)$. Next, bottleneck space–time point identification scans the grid–time domain and requires $\mathcal{O}(|G|)$ operations. The schedule construction stage then employs the island-style genetic algorithm. With population size P and I generations, and fitness evaluation proportional to the number of sensors, the dominant complexity of this stage scales as $\mathcal{O}(PI|S|)$. By combining the above components, the per-cycle computational cost can be expressed as

$$T_{\text{cycle}} = \mathcal{O}(|S||G|) + \mathcal{O}(|G|) + \mathcal{O}(PI|S|). \quad (88)$$

It can be observed that while the day-start computation is independent of runtime duration, the cycle-level complexity grows polynomially with the network size and grid resolution.

3) *Communication Overhead:*
Since optimization is centralized at the sink, communication overhead mainly arises from schedule dissemination. Let L_{sch} be the scheduling message size per sensor (in bits). The per-cycle communication cost is

$$C_{\text{cycle}} = \mathcal{O}(|S|L_{\text{sch}}). \quad (89)$$

No intersensor negotiation or iterative message exchange is required during optimization or execution. A single day-start broadcast of (τ, T_c) is amortized across cycles.

4) *System-Level Aggregation and Scalability:*
Let N_c be the number of cycles per day. The overall daily overhead becomes

$$T_{\text{day}} = T_{\text{PV}} + N_c T_{\text{cycle}}, \quad C_{\text{day}} = N_c C_{\text{cycle}}. \quad (90)$$

TABLE I
PSEUDOCODE OF THE PROPOSED MULTISTAGE OPTIMIZATION FRAMEWORK

Step	Procedure (execution node; key equations)
Input	S, R, w, $\mathcal{R} = \{r_1, \ldots, r_m\}$, (λ, γ), Ξ; MCTS (N, H, τ_0); GA (P, I); threshold λ_0.
Output	$\hat{p}^{PV}(t)$; (τ, T_c); $\{g_1^{tar}, \ldots, g_{c_2}^{tar}\}$; feasible schedule $s^\star$.
1	**Phase A:** Construct scenario tree T from historical data $\mathcal{D}$.
2	**for** $n = 1$ **to** N **do**: select by UCB (34); expand by (35); roll out to depth H.
3	Evaluate trajectory by (36)–(37); backpropagate statistics.
4	Aggregate rollouts to obtain committed PV profile $\hat{p}^{PV}(t)$ via (38)–(39).
5	**Phase B:** Compute harvested energy E^{cha} and balance by (52)–(53).
6	Determine slot length τ by (54); compute cycle parameters and obtain T_c by (55)–(60).
7	**for each** grid cell $g(x, y)$: compute farthest-point reduction (61) and cooperative detection probability (62).
8	**Phase C:** Compute usable energy and feasible radii by (67)–(75).
9	**if** preferred radius infeasible **then** back off by (73)–(75).
10	Compute grid feasibility $\lambda(x, y)$ and retain cells with $\lambda(x, y) \geq \lambda_0$ by (77)–(78).
11	Compute cooperative potential $W(x, y)$ by (79).
12	Run lexicographic DP recursion (80)–(87); backtrack to obtain target chain $\{g_1^{tar}, \ldots, g_{c_2}^{tar}\}$.
13	Initialize island-GA population (size P) encoding $M_{j,h}(\cdot)$.
14	**for** generation $= 1$ **to** I **do**: evaluate $q(s)$ by (18)–(21); repair violations of (23)–(27).
15	Apply genetic operators and elite migration; update population.
16	Output best schedule $s^\star$; broadcast $M_{j,h}(\cdot)$ to sensors; sensors execute locally over $h \in T_c$.

Overall, the proposed EBCS framework introduces a manageable system-level computational and communication overhead. Computation-intensive procedures are confined to the sink and executed at coarse time scales, while sensor nodes perform only lightweight slot-level operations without participating in iterative optimization or internode coordination. Consequently, the overall overhead grows in a controlled manner with network size, indicating that the framework remains practical and scalable for large-scale barrier coverage deployments.

Although the operational energy input considered in the proposed EBCS framework is PV-based, wind and hybrid renewable-energy systems are relevant to the broader environmental context of sustainable energy-harvesting sensor networks. Therefore, following insights from prior studies on small-scale wind turbines and social energy awareness [51], [52], we discuss the social and environmental implications of renewable-energy-powered WRSNs. In this article, wind energy is considered only as supplementary background for possible PV/wind hybrid extensions, whereas the optimization model, scheduling process, and simulations remain driven by day-ahead PV energy prediction. From the operational perspective, PV-powered WRSNs can reduce reliance on fossil-fuel-based electricity and support long-term energy-neutral sensing; from the broader renewable-energy perspective, wind and hybrid systems provide complementary context for sustainable sensor-network extensions. This clarification connects the supplementary wind-harvesting reference model in the Appendix II-B with the main text without expanding the technical scope of the proposed EBCS framework.

To further highlight the environmental relevance of renewable-energy-powered WRSNs, we provide an explicit discussion of CO_2 emissions and their role in the transition to cleaner energy resources, based on prior work [53]. In the operational setting of this article, PV-powered sensor operation reduces reliance on fossil-fuel electricity, thereby lowering CO_2 emissions associated with sensor operation and network maintenance. By enabling ENO at the sensor-node level, the proposed PV-driven scheduling framework helps maintain barrier coverage without drawing from carbon-intensive energy sources. Wind and hybrid renewable-energy systems are referenced as broader low-carbon context and possible extensions, but they are not part of the current optimization constraints, scheduling process, or simulation results. Collectively, these effects underscore the importance of considering CO_2 emissions when evaluating renewable-energy-powered WRSNs and demonstrate how such deployments can contribute to cleaner energy transitions.

For completeness, economic and environmental cost analyses including levelized cost of energy (LCOE), payback time metric (PBTM), and CO_2-related environmental costs are provided in the Appendix C.

The above discussion completes the proposed EBCS framework, including its algorithmic overhead and broader renewable-energy implications. The next section presents the experimental performance evaluation.

V. Performance Evaluations

This chapter will introduce performance verification.

Table II summarizes the seasonal performance of the four forecasting methods. Across all four seasons, MCTS consistently achieves the best accuracy, exhibiting the lowest MAE, RMSE, NRMSE, and Pinball Loss values. Its performance remains stable throughout the year, indicating strong robustness under varying seasonal patterns. CVSG ranks second and performs competitively, particularly in spring and summer. ENNT shows moderate error levels and remains consistently in the middle range of the four methods.

PAMA yields the highest errors across all metrics and seasons, with performance deterioration becoming more pronounced during winter, when forecasting conditions are typically more challenging. In general, the results show a gradual degradation from summer to winter, reflecting increased seasonal variability and prediction difficulty. Overall, the comparison demonstrates that MCTS provides the most accurate and stable performance year-round, outperforming all baselines across every seasonal setting.

TABLE II
Seasonal Performance Comparison Across Four Methods

Season	Method	MAE	RMSE	NRMSE	Pinball Loss
Spring	MCTS	0.0210	0.0280	0.0560	0.0510
	CVSG	0.0224	0.0297	0.0594	0.0530
	ENNT	0.0236	0.0315	0.0630	0.0560
	PAMA	0.0268	0.0362	0.0724	0.0600
Summer	MCTS	0.0173	0.0235	0.0470	0.0450
	CVSG	0.0181	0.0248	0.0496	0.0470
	ENNT	0.0196	0.0265	0.0530	0.0490
	PAMA	0.0220	0.0304	0.0608	0.0540
Autumn	MCTS	0.0190	0.0268	0.0536	0.0480
	CVSG	0.0202	0.0284	0.0568	0.0500
	ENNT	0.0217	0.0301	0.0602	0.0520
	PAMA	0.0245	0.0340	0.0680	0.0580
Winter	MCTS	0.0249	0.0368	0.0736	0.0560
	CVSG	0.0262	0.0389	0.0778	0.0590
	ENNT	0.0274	0.0405	0.0810	0.0610
	PAMA	0.0308	0.0447	0.0894	0.0670

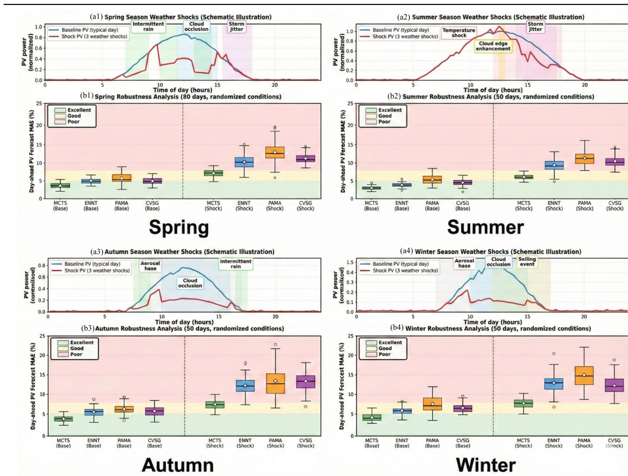

Fig. 13. Seasonwise robustness of day-ahead PV prediction under abrupt, nonhistorical microclimate variations. (a1) Spring season weather shocks (schematic illustration). (b1) Spring robustness analysis (80 days, randomized conditions). (a2) Summer season weather shocks (schematic illustration). (b2) Summer robustness analysis (50 days, randomized conditions). (a3) Autumn season weather shocks (schematic illustration). (b3) Autumn robustness analysis (50 days, randomized conditions). (a4) Winter season weather shocks (schematic illustration). (b4) Winter robustness analysis (50 days, randomized conditions).

To evaluate the robustness of day-ahead PV prediction under abrupt and nonhistorical microclimate variations, we conduct a seasonwise robustness study using four representative seasons (spring, summer, autumn, and winter). For each season, three typical classes of abrupt weather shocks are identified according to common microclimate phenomena observed in real-world PV systems, including cloud occlusion, intermittent precipitation, aerosol haze, storm-induced irradiance jitter, temperature shocks, and soiling-related degradation.

For each season, the upper subfigure in Fig. 13 provides a schematic illustration of a representative daily PV profile together with injected weather shocks, whose purpose is to visually demonstrate the temporal characteristics and physical manifestations of different microclimate disturbances.

Importantly, this schematic curve is not used for statistical evaluation. The quantitative robustness results reported in the lower subfigures are obtained from 50 independent days per season, where the baseline PV profiles are drawn from real measured data and the shock parameters (occurrence time, duration, and intensity) are randomized across days. All methods perform one day-ahead prediction per day, and the resulting forecast errors are aggregated across days to form the boxplot statistics. This protocol ensures that the reported distributions reflect robustness against diverse, nonrepetitive perturbations rather than repeated predictions on a single realization.

From a standalone perspective, the MCTS-based PV prediction already exhibits a stable and well-bounded error distribution across all four seasons, even under abrupt microclimate disturbances. As shown in Fig. 13, the interquartile ranges of MCTS remain compact under shock conditions, and the median errors increase moderately without exhibiting heavy tails or extreme outliers. This behavior indicates that the proposed MCTS model does not rely on overly optimistic assumptions about smooth irradiance evolution and can maintain consistent predictive performance when exposed to sudden, irregular perturbations.

When compared with DL-based counterparts (ENNT, PAMA, and CVSG), the robustness advantage of MCTS becomes more pronounced under shock conditions. While all methods experience performance degradation due to nonhistorical disturbances, the error distributions of the neural models exhibit larger dispersion and upward shifts in median MAE, particularly in summer and winter scenarios where cloud-edge enhancement, storm jitter, and soiling effects dominate. In contrast, MCTS consistently yields lower median errors and narrower distributions across all seasons.

This robustness advantage stems from the fundamental modeling philosophy of MCTS. Rather than learning a fixed functional mapping from historical data, MCTS explicitly constructs a scenario tree that enumerates multiple plausible future irradiance trajectories through stochastic rollouts. The use of progressive widening allows the search to adaptively allocate exploration budget to rare but high-impact branches, while the final day-ahead PV estimate is obtained via risk-aware aggregation across the tree. As a result, abrupt microclimate variations—although not seen during training—are implicitly covered by alternative branches in the search space, preventing single-point forecast collapse. By contrast, DL models trained on historical distributions tend to extrapolate poorly when confronted with out-of-distribution weather shocks, leading to amplified errors and higher variance. These results collectively demonstrate that the proposed MCTS-based PV prediction offers superior robustness under abrupt, nonhistorical microclimate variations.

Fig. 14 compares the surveillance quality achieved by four methods (EBCS, BCRAS, MSQBE, and NEDA) under varying numbers of deployed sensors and available sensing radii. Across all four subfigures, EBCS consistently attains the highest surveillance quality, demonstrating strong robustness when both sensing diversity and sensor density increase. MSQBE ranks second, followed by BCRAS, while NEDA shows the

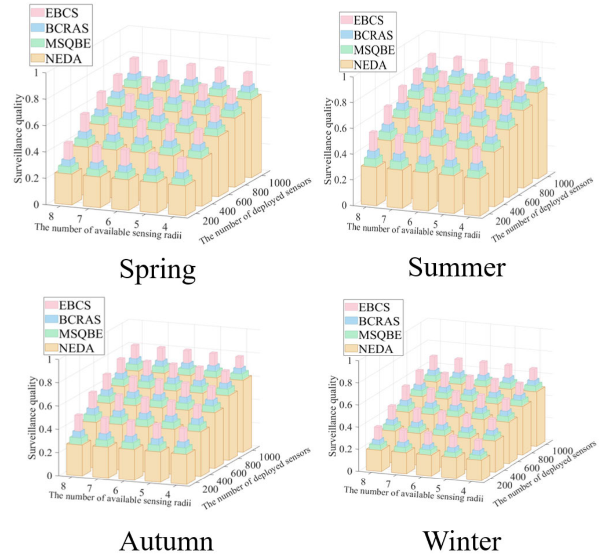

Fig. 14. Comparison of the surveillance quality achieved by four methods.

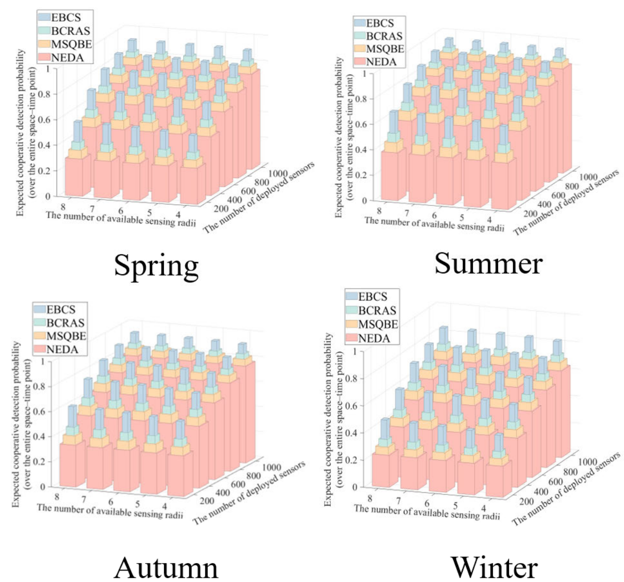

Fig. 15. Comparison of the ECPD achieved by four algorithms.

lowest performance throughout all tested configurations. The relative ordering of the methods remains stable across the entire parameter range, indicating that the comparative advantages of each algorithm are not sensitive to changes in network size or sensing flexibility.

Another clear trend is that surveillance quality improves monotonically with both the number of sensors and the number of sensing radii. Larger sensor populations provide greater spatial redundancy, while richer sensing radius sets enhance coverage adaptability, benefiting all methods. However, the gap between the four methods persists and even becomes more evident at higher sensor densities, highlighting the superior scalability of EBCS. Overall, these results demonstrate that EBCS achieves the most reliable surveillance performance and maintains its advantage across a broad spectrum of deployment conditions.

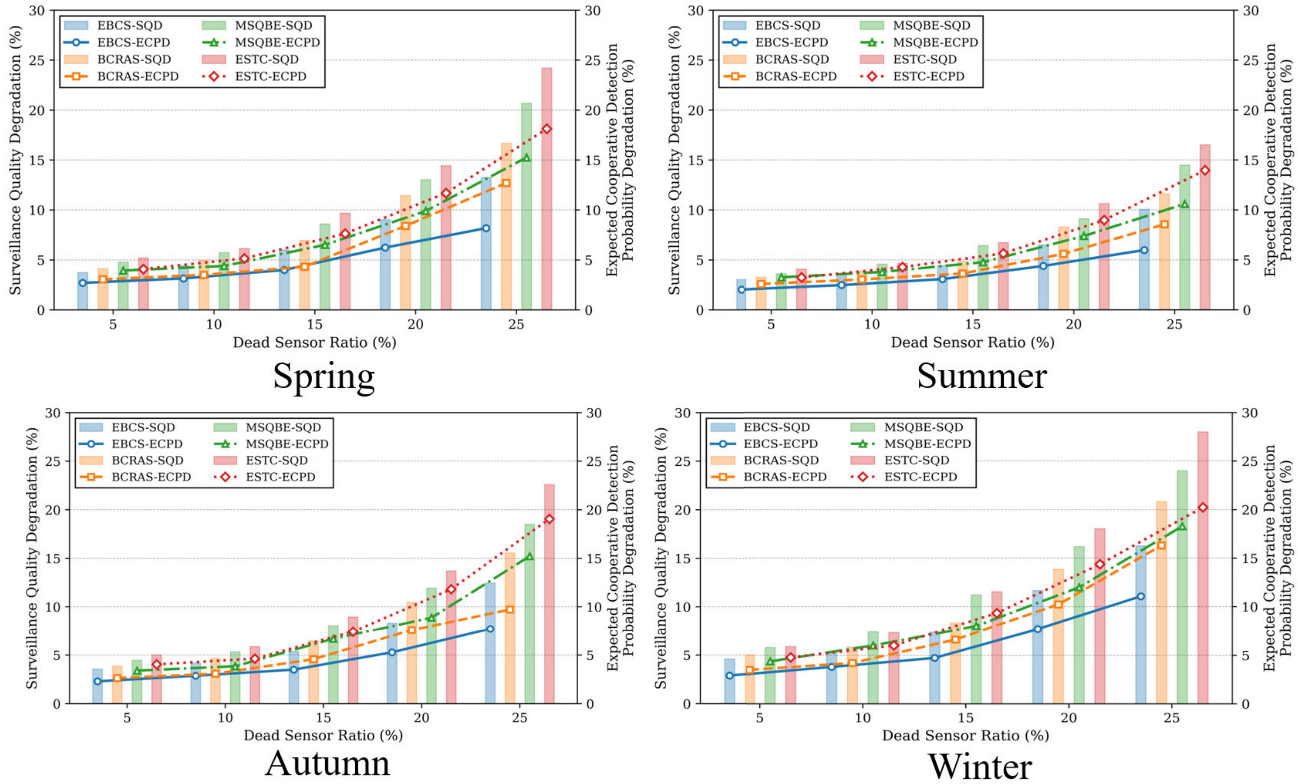

Fig. 16. Trends of SQD and ECPD under different sensor mortality rates.

Fig. 15 presents the expected cooperative detection probability (ECPD) achieved by four algorithms (EBCS, BCRAS, MSQBE, and NEDA) under different numbers of deployed sensors and available sensing radii. Across all four subfigures, MSQBE exhibits the highest detection probability, demonstrating strong robustness as both sensing diversity and network size increase. EBCS ranks second with consistently high performance, whereas BCRAS shows moderate levels. NEDA yields the lowest probability among the four methods but still benefits from larger sensor populations and richer sensing-radius sets. The ordering of the algorithms remains stable across all parameter ranges, indicating that their relative performance is insensitive to variations in deployment scale or sensing flexibility.

A clear monotonic trend is observed: cooperative detection probability increases as the number of sensors or the number of available radii grows. Larger sensor populations enhance spatial coverage redundancy, while more sensing radii improve adaptability to environmental and geometric conditions. Although all methods experience performance gains, the gaps between them become more pronounced for higher sensor densities, highlighting the superior scalability of MSQBE and EBCS. Overall, the results show that MSQBE delivers the most reliable cooperative detection capability, followed by EBCS, while BCRAS and NEDA trail behind across all tested configurations.

Fig. 16 illustrates the impact of dead sensor ratio on two performance degradation metrics: surveillance quality degradation (SQD) and ECPD. Across all four subfigures, both SQD and ECPD increase monotonically as more sensors fail, indicating that system-level performance degrades progressively with reduced sensing coverage. Among the algorithms, EBCS consistently exhibits the lowest SQD and ECPD across the entire 0%–27% death range, demonstrating strong resilience to sensor loss. BCRAS follows with moderate degradation, while MSQBE shows noticeably higher sensitivity. ESTC suffers the most severe degradation, with rapid increases in both SQD and ECPD, reflecting limited robustness under sensor failures.

Despite variations among the four scenarios, the relative ranking of the methods remains stable

$$\text{EBCS} < \text{BCRAS} < \text{MSQBE} < \text{ESTC}$$

in terms of performance degradation. This consistent ordering suggests that the degradation behavior is dominated by the intrinsic design of each scheduling strategy rather than scenario-dependent factors. Overall, EBCS demonstrates superior robustness under increasing sensor mortality, while ESTC is the most vulnerable, with degradation intensifying sharply as the dead sensor ratio grows.

Fig. 17 examines how the grid side length w influences the mean absolute error (MAE) of cooperative detection for different minimum sensing radii $r_{\min}$, while also reporting runtime per scene. Across all curves, MAE grows approximately linearly with increasing grid size, since a larger w coarsens the spatial resolution and reduces the fidelity of probabilistic aggregation. Methods using smaller $r_{\min}$ values (e.g., 10–14 m) exhibit higher MAE under the same w, as limited sensing coverage amplifies resolution-induced uncertainty. Conversely, larger sensing radii (22–30 m) maintain lower MAE and slower

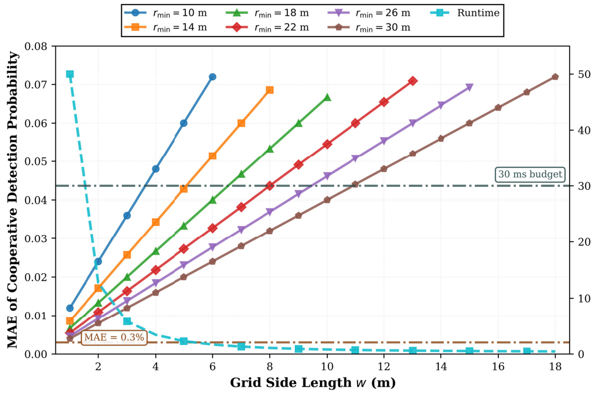

Fig. 17. Grid side length w influences the MAE of cooperative detection for different minimum sensing radii $r_{\min}$.

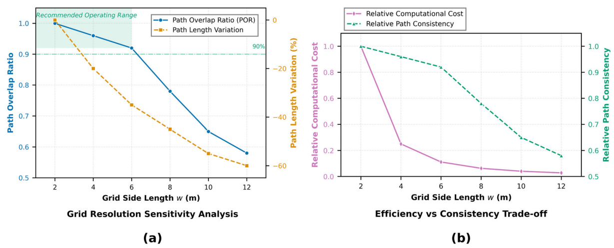

Fig. 18. Grid resolution sensitivity analysis for weakest-path identification and coverage optimality.

degradation rates, showing that stronger geometric coverage mitigates grid discretization effects.

The runtime curve demonstrates that computational cost remains extremely low across all grid sizes, staying well below the 30-ms real-time budget. Runtime decreases rapidly for small w due to reduced neighborhood evaluations, and stabilizes under 2 ms for $w \geq 6$ m. This indicates that the proposed method achieves real-time feasibility even under dense scene configurations. Overall, the results highlight a tradeoff between spatial resolution and detection accuracy, while confirming that runtime is negligible compared to accuracy-driven considerations.

To clarify how grid resolution affects weakest-path identification and coverage optimality, we conduct a grid resolution sensitivity analysis by varying the grid side length w while keeping the sensor deployment, PSM, and optimization pipeline unchanged. We consider $w \in \{2, 4, 6, 8, 10, 12\}$ m and treat the finest discretization ($w_{\text{ref}} = 2$ m) as the reference for geometric consistency evaluation. The weakest-path geometry consistency is quantified by the POR, defined as the fraction of path cells under resolution w that overlap with those on the reference path. In addition, the relative path length variation (normalized by the reference path) is reported to characterize geometric simplification as the grid becomes coarser.

As shown in Fig. 18(a), the POR decreases smoothly as w increases. For moderate grid resolutions ($w \leq 6$ m), the identified weakest paths remain highly consistent, with POR staying above 0.9, indicating that the dominant bottleneck structure is largely preserved under reasonable discretization. When the grid becomes coarser ($w \geq 8$ m), POR declines more noticeably, which is expected since reduced spatial resolution progressively smooths out local coverage minima and may shift the geometric location of the weakest path. Meanwhile, the path length exhibits a gradual reduction bounded within approximately 60% relative to the finest-grid baseline, reflecting geometric simplification rather than barrier collapse. Even under coarse discretization, a continuous left-to-right weakest path is still maintained, albeit with reduced geometric fidelity.

To further interpret the efficiency–reliability tradeoff induced by grid resolution, Fig. 18(b) reports the relative computational cost and the relative path consistency as functions of w. As expected, finer grids incur higher computational cost due to a larger candidate set, but provide stronger weakest-path consistency. Conversely, coarser grids substantially reduce computational burden at the expense of gradually decreased path consistency. Overall, the results confirm that the influence of grid resolution on weakest-path identification manifests as a progressive and interpretable tradeoff rather than abrupt degradation. In our setting, a moderate grid side length range $w \in [2, 6]$ m provides a favorable balance between geometric fidelity, coverage reliability, and computational efficiency.

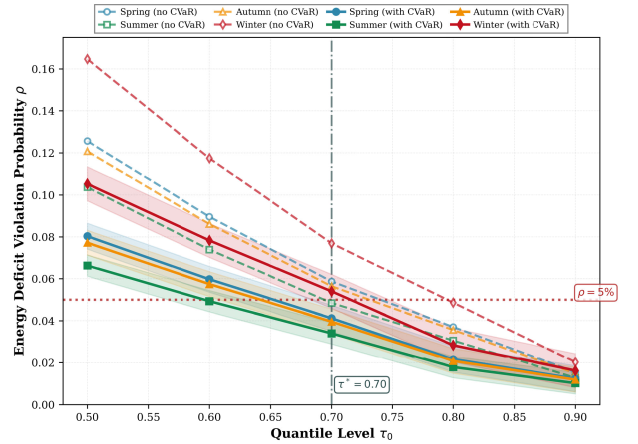

Fig. 19. Effect of quantile level on energy deficit violation probability with and without CVaR across seasons.

Fig. 19 analyzes how the energy deficit violation probability ρ varies with the quantile level τ_0 under four seasonal energy profiles, comparing models with and without CVaR-based robust regularization. Across all seasons, ρ decreases monotonically as τ_0 increases, reflecting the stronger conservativeness achieved at higher quantile thresholds. Incorporating CVaR consistently lowers ρ for every season and every quantile level, demonstrating that CVaR effectively suppresses tail-risk energy shortages and significantly improves reliability.

Among the seasons, winter exhibits the highest violation probabilities due to the lowest solar energy availability and strongest daily fluctuations. Spring and autumn show moderate violation levels, while summer yields the lowest risk overall. The reference limit $\rho = 5\%$ and the highlighted operating point $\tau_0^\star = 0.70$ show that CVaR-based control meets the reliability requirement in all seasons, whereas the non-CVaR version fails to meet the 5% risk threshold in winter and marginally violates it in spring and autumn. These results confirm the effectiveness and seasonal robustness of integrating CVaR into energy-aware scheduling.

To quantitatively analyze how PV prediction errors affect energy neutrality and barrier coverage performance, we

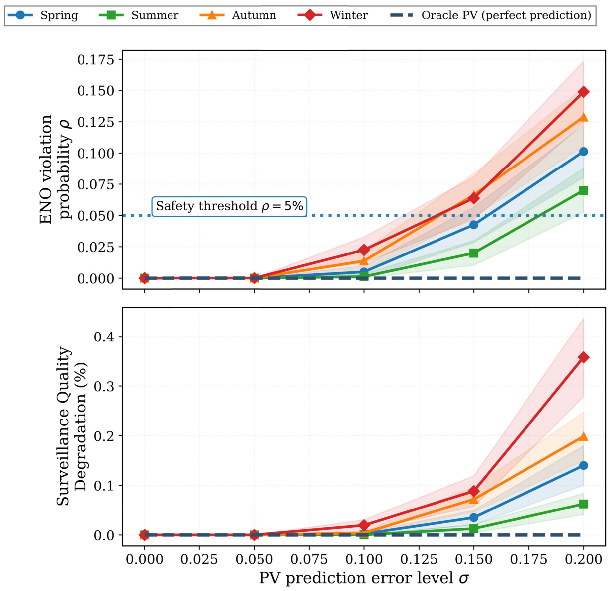

Fig. 20. Impact of PV prediction errors on energy neutrality and barrier coverage performance.

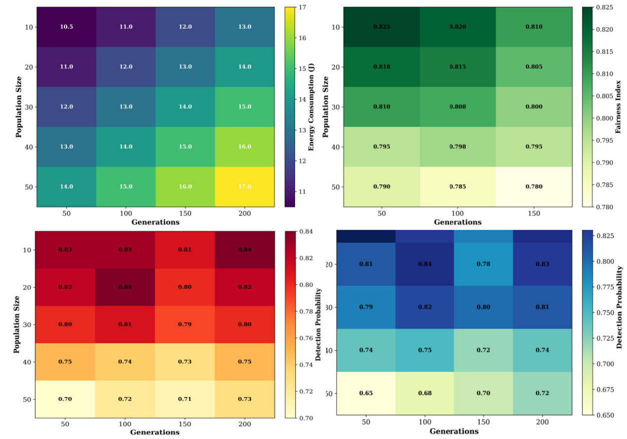

Fig. 21. Joint influence of population size and generations on energy consumption, fairness, feasibility, and detection probability.

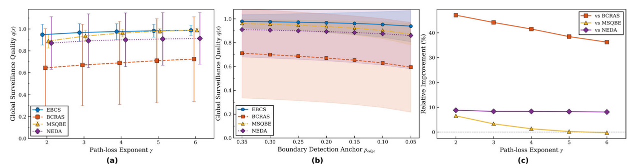

Fig. 22. Generalizability of the proposed EBCS framework across different sensing environments characterized by PSM path-loss parameters.

conduct a Monte Carlo-based sensitivity evaluation under stochastic PV perturbations. Let $P(t)$ be the realized PV profile of a day and $\hat{P}(t)$ the corresponding day-ahead forecast used for schedule construction. Different uncertainty levels are emulated by injecting multiplicative perturbations with controlled intensity σ into the day-ahead PV forecasts. For each σ, the day-ahead sensing schedule is constructed at the fixed operating point $\tau_0 = \tau^*$ (see Fig. 19) with CVaR-based risk control, and then executed against the realized PV profiles. An energy-neutrality violation is recorded when the harvested energy is insufficient to support the planned sensing energy consumption, and the ENO violation probability ρ is computed as the fraction of trials with such violations. When an energy shortfall occurs, sensors are forced to reduce their active durations to preserve feasibility, which yields a degraded executed schedule. The resulting performance loss is quantified as the *SQD* (%), defined as the relative degradation compared to the ideal execution without energy deficits. This procedure enables a quantitative assessment of how PV forecasting inaccuracies propagate from the energy domain to schedule execution and, ultimately, to the achieved barrier surveillance quality.

Fig. 20 illustrates the resulting ENO violation probability and SQD as functions of the PV prediction error level σ, evaluated separately for four seasons. As shown in the upper subfigure, the ENO violation probability increases monotonically with σ, indicating that larger prediction errors lead to more frequent energy shortfalls during execution. Clear seasonal disparities can be observed, with winter being the most sensitive due to its lower and more volatile energy availability. The dashed horizontal line indicates the safety threshold $\rho = 5\%$, below which long-term ENO is considered acceptable, while the oracle PV curve corresponds to the ideal case of perfect day-ahead prediction and serves as an upper-bound reference.

The lower subfigure reports the corresponding SQD, measured as the percentage loss relative to the ideal execution without energy deficits. As σ increases, mismatches between the planned and executable schedules become more pronounced, resulting in progressively larger quality degradation. Consistent with the ENO analysis, winter exhibits the steepest performance loss, whereas summer remains relatively robust. These results quantitatively demonstrate how PV prediction errors propagate through the proposed framework, jointly affecting both energy neutrality and barrier coverage performance.

Fig. 21 presents the sensitivity of four key performance indicators to the algorithmic parameters population size and number of generations. In the energy consumption heatmap (top-left), energy usage increases steadily with both parameters, suggesting that larger populations and longer evolutionary procedures lead to more computationally intensive schedules. The fairness index (top-right) displays an opposite trend: fairness decreases gradually as population size grows, indicating that overly large populations may over-exploit energy-rich sensors and reduce balance across the network.

The feasibility heatmap (bottom-left), reflecting the proportion of feasible schedules, shows that feasibility declines with increasing population size, with values dropping from above 0.83 to near 0.70. This suggests that excessively large search spaces may hinder convergence toward energy-sustainable solutions. In contrast, the detection probability (bottom-right) decreases moderately with population size but improves slightly with more generations, indicating that detection performance benefits from iterative refinement but is negatively impacted by overly large populations. Taken together, the results show that moderate parameter settings (e.g., population size 20–30 and generations 100–150) provide the best overall balance between energy efficiency, fairness, feasibility, and detection reliability.

To assess the generalizability of the proposed framework with respect to environment-dependent sensing parameters, we conduct a sensitivity study on the PSM path-loss exponent γ. Fig. 22(a) illustrates the relative improvement of the proposed EBCS framework over the baseline schemes as the path-loss exponent γ varies from 2 to 6. It can be observed that EBCS consistently achieves substantial performance gains over BCRAS across the entire range of γ, although the relative improvement gradually decreases as the sensing attenuation becomes steeper. In contrast, the performance gap between EBCS and MSQBE diminishes as γ increases and becomes marginal under highly attenuated environments, while a stable improvement over NEDA is preserved. These results indicate that the superiority of EBCS does not rely on a specific sensing decay exponent and remains robust under diverse environmental conditions.

Fig. 22(b) reports the absolute global surveillance quality $q(s)$ achieved by different algorithms under varying path-loss exponents γ. As γ increases, moderate variations in the absolute performance can be observed for all methods; however, the relative ordering among the algorithms remains unchanged. EBCS consistently attains the highest surveillance quality across all considered values of γ, followed by MSQBE, NEDA, and BCRAS. This observation confirms that the effectiveness of the proposed bottleneck-aware and cycle-level cooperative scheduling strategy is insensitive to the specific choice of the path-loss exponent and generalizes well across sensing environments with different attenuation characteristics.

Fig. 22(c) further examines the robustness of different scheduling strategies with respect to the sensing attenuation strength by varying the boundary detection anchor p_{edge}, which is directly related to the path-loss coefficient λ. As p_{edge} decreases, corresponding to increasingly adverse sensing environments, the global surveillance quality of all methods degrades gradually. Notably, EBCS exhibits the slowest performance degradation and consistently maintains the highest surveillance quality over the entire range of p_{edge}. In comparison, the baseline schemes suffer from more pronounced performance deterioration as the sensing conditions worsen. These results demonstrate that the proposed framework is less sensitive to variations in the path-loss coefficient and preserves its performance advantage without requiring environment-specific parameter tuning.

Overall, the results in Fig. 22(a)–(c) collectively confirm that the proposed EBCS framework exhibits strong generalizability across a wide spectrum of sensing environments characterized by different path-loss parameters, and its performance superiority is not contingent on a particular choice of the PSM coefficients.

To assess the robustness of the proposed framework beyond idealized settings, we conduct a dedicated robustness study that explicitly considers execution-level imperfections. Specifically, we evaluate performance under imperfect synchronization and packet loss by executing the planned schedules with perturbations, without replanning, while keeping all methods under identical conditions.

Two metrics are reported. *SQD* measures the relative degradation of the weakest space–time barrier, while *effective cooperative probability degradation* captures the relative loss in average cooperative detection probability. Both are computed per trial against each method's ideal baseline and then averaged.

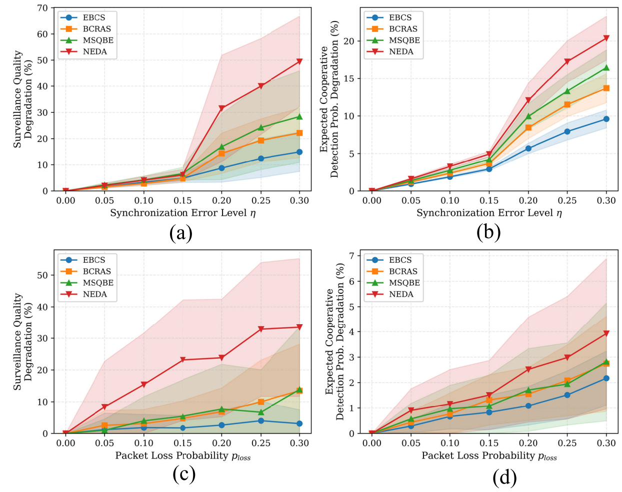

Fig. 23. Robustness evaluation under nonideal execution: impact of imperfect synchronization and packet loss. (a) SQD versus synchronization error. (b) ECPD versus synchronization error. (c) SQD versus packet loss. (d) ECPD versus packet loss.

As shown in Fig. 23(a) and (b), both metrics increase roughly linearly under small synchronization errors because timing offsets mainly attenuate within-slot sensing contributions. When errors grow larger, degradation accelerates due to slot misalignment that disrupts weakest-path continuity; accordingly, SQD increases faster than effective cooperative probability degradation. EBCS consistently exhibits the smallest degradation, while NEDA is the most sensitive.

Fig. 23(c) and (d) shows a monotonic increase in both metrics with packet loss probability. Again, SQD is more sensitive, indicating that localized execution failures can severely weaken the weakest space–time bottleneck even when average detection degrades moderately. EBCS remains the most robust across all packet loss levels.

EBCS outperforms BCRAS, MSQBE, and NEDA because it explicitly strengthens the weakest space–time bottleneck and maintains higher redundancy and slack, reducing reliance on a few critical sensors or slots and limiting the impact of individual execution failures. In contrast, NEDA's energy-driven activation yields thinner coverage margins and lower redundancy, so delayed or lost commands more readily expose already-weak space–time points, leading to the fastest degradation.

Overall, execution imperfections affect average sensing performance moderately but can markedly degrade weakest-path surveillance quality, and higher spatial redundancy improves robustness.

Beyond the above experimental evaluation, we discuss the gap between simulation assumptions and practical deployment constraints in real-world WRSNs, to clarify the applicability of the proposed EBCS framework under realistic operating conditions. Although EBCS is evaluated through simulations, real deployments inevitably involve sensing noise, communication delays, and hardware limitations. The following discussion

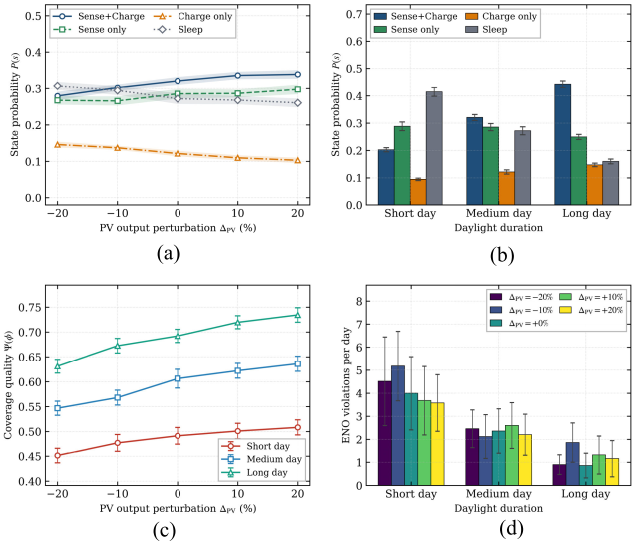

Fig. 24. Effect of PV output perturbation and daylight duration on WRSN node decision probabilities. (a) State probability versus PV perturbation (medium day). (b) State probability across daylight regimes. (c) Network coverage versus PV perturbation. (d) Energy-neutrality violations.

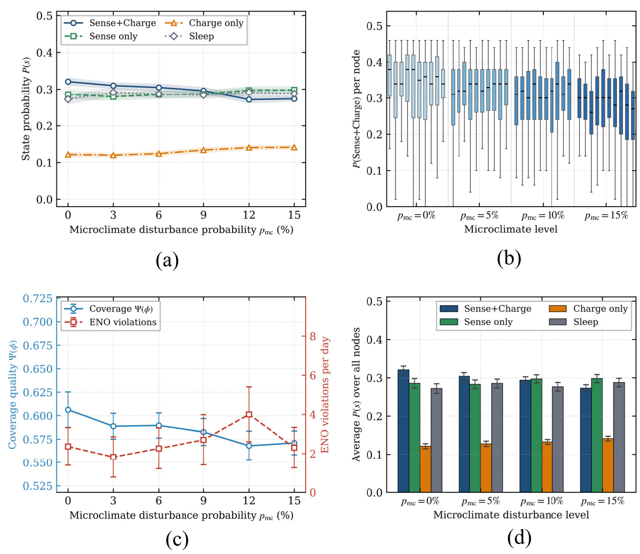

Fig. 25. Impact of microclimate disturbance probability on WRSN node state distributions. (a) State probability versus microclimate disturbance. (b) Per-node variability of sense + charge probability (ten heterogeneous nodes per group). (c) Coverage and ENO violations versus microclimate level. (d) Aggregated state probability at key levels.

explains how these factors are abstracted in the proposed design and why they do not invalidate the effectiveness of the scheduling framework. Sensing uncertainty and environmental noise are captured by the PSM, which characterizes detection performance statistically rather than via idealized binary coverage. Path-loss and sensing-decay parameters accommodate heterogeneous propagation and measurement noise, while cooperative detection aggregation exploits spatial redundancy to mitigate localized sensing impairments. Communication delays and synchronization imperfections are addressed at the system level. EBCS adopts a day-ahead scheduling paradigm in which sensing schedules are computed in advance and executed locally by sensor nodes. By avoiding frequent real-time coordination, the framework reduces sensitivity to delayed

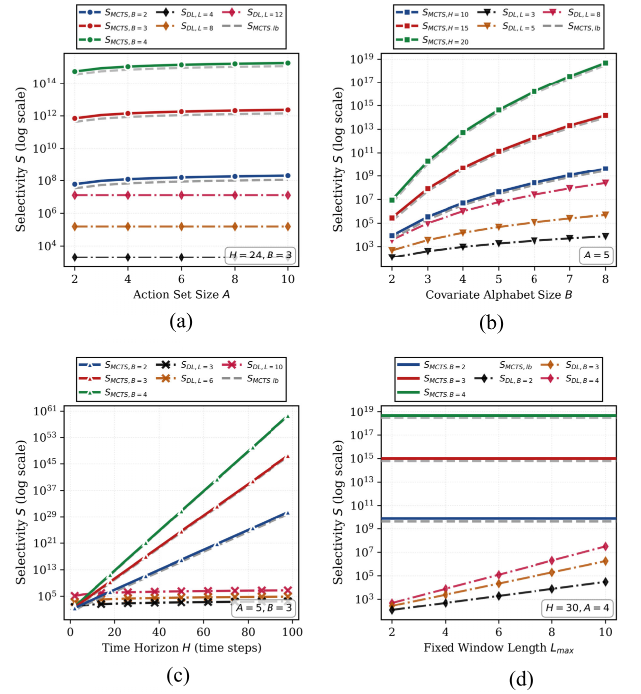

Fig. 26. Experiment of Theorem 4. (a) Impact of action set size A. (b) Impact of alphabet size B. (c) Impact of time horizon H. (d) Impact of window length L_max.

or outdated control messages and remains robust under nonnegligible latency or intermittent connectivity. Hardware constraints are handled through a sink-assisted hierarchical execution structure. Computationally intensive tasks, including PV energy prediction, cooperative detection evaluation, and schedule optimization, are executed at the sink, whereas sensor nodes only perform lightweight slot-level state switching. This separation ensures compatibility with resource-constrained hardware and avoids excessive in-network computation.

In long-term deployments, battery aging, leakage, and PV panel degradation introduce additional nonideal energy effects. Battery aging and leakage reduce effective capacity and charge–discharge efficiency, while panel degradation leads to a gradual decline in harvested energy yield. Although these effects are not explicitly modeled, they evolve over long time scales and can be interpreted as slow systematic variations in the available energy budget. Since EBCS relies on periodic day-ahead energy estimation and cycle-level energy balancing, the cumulative impact of long-term degradation can be absorbed through updated daily energy budgeting without altering the core scheduling logic or coordination mechanisms. Consequently, stable operation can be maintained under realistic long-term energy degradation with minimal additional overhead.

To assess the robustness and decision-making behavior of WRSN nodes under variable environmental conditions, we conducted a sensitivity analysis examining how PV output perturbations and daylight duration, as well as microclimate disturbances, influence node scheduling decisions. This experiment aims to quantify the responsiveness of the EBCS scheduling algorithm to environmental variations, providing insights into the reliability and ENO of the network.

Following methodologies used in sensitivity analyses for hybrid energy systems [54], we simulated PV output fluctuations from −20% to +20% and daylight durations representing short, medium, and long days, recording the probability of each node selecting one of four possible states: sense + charge, sense only, charge only, and sleep. Microclimate disturbances with varying probabilities (0%, 5%, 10%, and 15%) were introduced to evaluate their effect on decision distributions. Fig. 24 shows the effect of PV output perturbation and daylight duration on node decision probabilities, while Fig. 25 demonstrates how increasing microclimate disturbance probabilities impact node states. Under a medium-daylight profile, sense + charge increases with PV input, while sleep and charge-only decrease, showing energy sufficiency influences wake/sleep decisions. Daylight duration has a stronger impact than PV magnitude, with sleep probability decreasing and sense + charge increasing under longer days.

In Fig. 25, microclimate disturbances cause moderate mean shifts but large internode variability. Some nodes defer sensing earlier under higher disturbances, illustrating sensitivity to environmental heterogeneity. Overall, both PV availability and microclimate variability critically shape node scheduling, and the EBCS algorithm effectively maintains ENO while preserving reliable barrier coverage.

VI. Conclusion

This article presented the EBCS algorithm to address the dual challenges of reliable barrier surveillance and long-term energy sustainability in WRSNs equipped with adjustable sensing radii. Motivated by the limitations of traditional Boolean sensing, fixed-radius models, and simplified energy assumptions, EBCS integrates three key designs to enhance monitoring quality under realistic operational conditions.

First, to cope with the uncertainty of solar energy availability, an MCTS framework was introduced to construct probabilistic PV energy scenarios. This enables more accurate prediction of next-day solar supply by inferring energy distributions from historically similar conditions. Second, a periodic energy-balancing mechanism was developed to allocate activation duration across sensing cycles based on predicted energy and sensor-specific consumption under different radii, ensuring energy neutrality while avoiding overload. Third, a grid-based cooperative sensing model was constructed to quantify probabilistic joint detection, and an Island-GA was designed to prioritize scheduling for sensors that contribute most to weak spatiotemporal regions.

Extensive simulations demonstrate that the proposed EBCS significantly outperforms existing approaches in terms of energy utilization efficiency, fairness, cooperative detection probability (ECPD), and overall barrier surveillance quality. Representative numerical results show that the worst case barrier coverage quality $\bar{\Psi}^{\min}$ reaches 0.92 under high solar variability, with a DR-RMSE of 7.5% under abrupt PV shocks, and long-term energy-neutral violation occurs for only 2.3 days per node on average. Under a 0%–27% dead sensor ratio, the SQD increases only by 2%–5%, indicating strong robustness. Grid resolution sensitivity shows POR above 0.9 for $w \leq 6$ m, ensuring geometric consistency. CVaR-based control maintains ENO violation probability ρ below 5% in all seasons. These quantitative results directly support the conclusions on the reliability and effectiveness of the framework.

Future work will explore distributed implementations of the proposed EBCS for large-scale deployments, incorporate machine learning techniques for adaptive sensing-radius selection, and investigate reinforcement learning-based scheduling under partially observable intruder behaviors.

Appendix I
Formal Statement and Experimental Validation of Theorem 4

Theorem 5: (Selectivity Advantage: MCTS Versus Fixed-Window Deep Models; Time-Step Form).

Setup: Consider a day with H time steps and a finite discretization of covariates. Let each time step's meteorological/terrain feature be encoded as a symbol in an alphabet $\mathcal{X}$ of size $B \geq 2$. For each time step h, the action set has size A_h, and write $A := \min_h A_h \geq 2$. A day policy maps a full-day covariate path $\Xi = (\xi_1, \ldots, \xi_H) \in \mathcal{X}^H$ to a sequence of actions $(a_1, \ldots, a_H)$ with $a_h \in \mathcal{A}_h$. Define the selectivity (combinatorial capacity) of a policy class $\mathcal{H}$ as $S(\mathcal{H}) := \log_A |\mathcal{H}|$.

Fixed-Window DL Classes: For window length L, a fixed-window class $\mathcal{H}_{\mathrm{DL}}(L)$ restricts a_h to be a function of the last L symbols only, i.e., $a_h = \varphi_h(\xi_{h-L:h-1})$ (with padding for $h \leq L$). The number of distinct per-time-step maps is at most A^{B^L}. Hence,

$$|\mathcal{H}_{\mathrm{DL}}(L)| \leq A^{HB^L}, \quad S(\mathcal{H}_{\mathrm{DL}}(L)) \leq HB^L. \tag{A1}$$

The three DL baselines are instances of $\mathcal{H}_{\mathrm{DL}}(L_j)$ with fixed L_j. Their union obeys

$$S\left(\bigcup_j \mathcal{H}_{\mathrm{DL}}(L_j)\right) \leq \max_j S\left(\mathcal{H}_{\mathrm{DL}}(L_j)\right) \leq HB^{L_{\max}}, \quad L_{\max} := \max_j L_j. \tag{A2}$$

MCTS Class: The MCTS-induced class $\mathcal{H}_{\mathrm{MCTS}}$ permits per-time-step decisions to depend on variable-length history and the full day-ahead path. Distinct policies can be indexed by functions of prefixes $\xi_{1:h}$. A counting lower bound is

$$|\mathcal{H}_{\mathrm{MCTS}}| \geq \prod_{h=1}^{H} A^{B^h} \geq A^{\sum_{h=1}^{H} B^h} \geq A^{HB^{H-1}}, \quad B \geq 2 \tag{A3}$$

which yields

$$S(\mathcal{H}_{\mathrm{MCTS}}) \geq \sum_{h=1}^{H} B^h \geq HB^{H-1}. \tag{A4}$$

Claim (Strict Selectivity Gap): If $H > L_{\max}$ and $B \geq 2$, then,

$$S(\mathcal{H}_{\mathrm{MCTS}}) > S\left(\bigcup_j \mathcal{H}_{\mathrm{DL}}(L_j)\right) \tag{A5}$$

and the gap grows at least as $HB^{H-1}\ H\ B^{L_{\max}}$.

Fig. 26 consists of four subplots that jointly illustrate the selectivity separation predicted by Theorem 4 between the proposed MCTS-based predictor and the three fixed-window

DL models [7], [8], [22]. In Fig. 26(a), *impact of action set size* A, we vary the minimum action set size A while fixing the time horizon $H = 24$ and the alphabet size $B = 3$. For all tested values of A, the selectivity of MCTS, $S_{\text{MCTS},B}$, is several orders of magnitude higher than that of the fixed-window DL class, $S_{\text{DL},L}$, and the gap widens as A increases. The solid curves for $B \in \{2, 3, 4\}$ also lie well above the theoretical lower bound $S_{\text{MCTS,lb}}$, confirming the multiplicative contribution of the action branching factor predicted by (A3) and (A4). Fig. 26(b), *impact of alphabet size* B, studies the effect of enlarging the covariate alphabet while keeping $A = 5$. As B grows from 2 to 8, the MCTS selectivity curves $S_{\text{MCTS},H}$ (for horizons $H \in \{10, 15, 20\}$) increase extremely rapidly on the log scale, reflecting the B^h term in (A3), whereas the curves for fixed-window DL with lengths $L \in \{3, 5, 8\}$ grow much more slowly and remain far below $S_{\text{MCTS,lb}}$. This behavior matches the upper bound $S(\mathcal{H}_{\text{DL}}) \le HB^{L_{\max}}$ in (A2), where $L_{\max} \ll H$. Fig. 26(c), *impact of time horizon* H, varies the horizon from 5 to 100 under $A = 5$ and $B = 3$. Here the MCTS selectivity $S_{\text{MCTS},B}$ grows almost linearly on the log scale (i.e., exponentially in H), while the fixed-window DL classes with $L \in \{3, 6, 10\}$ increase only modestly and stay close to their corresponding upper bounds. As H becomes large, the gap between $S_{\text{MCTS},B}$ and $S_{\text{DL},L}$ explodes, which is precisely the $HB^{H-1} - HB^{L_{\max}}$ growth predicted by Theorem 4. Finally, Fig. 26(d), *impact of window length* $L_{\max}$, directly compares the effect of increasing the maximum window size of DL models when $H = 30$ and $A = 4$. In this subplot, $S_{\text{MCTS},B}$ (horizontal solid lines) denotes the selectivity of the MCTS policy class for a fixed alphabet size $B \in \{2, 3, 4\}$, which is independent of $L_{\max}$ by construction, while $S_{\text{DL},B}$ (dashed and dash–dotted lines with markers) denotes the selectivity of the corresponding fixed-window DL class with the same alphabet size B and a maximum window length $L_{\max}$ shown on the x-axis. Thus, unlike in Fig. 26(a)–(c), where the DL curves are indexed by the window length L and written as $S_{\text{DL},L}$, here we index the DL curves by the alphabet size and write $S_{\text{DL},B}$ to emphasize that each family of curves shares the same B while $L_{\max}$ varies. The fixed-window selectivity $S_{\text{DL},B}$ increases with $L_{\max}$, but even at $L_{\max} = 10$ it remains several orders of magnitude below the flat MCTS curves $S_{\text{MCTS},B}$, providing further evidence that removing the fixed-window constraint leads to a dramatically larger policy class.

Appendix II
PV Energy Modeling and Supplementary Wind-Harvesting Reference Model

To clarify the energy input calculation used in the proposed scheduling and barrier coverage simulation, Appendix II-A presents the PV energy model adopted in this study. Appendix II-B further provides a standard wind-harvesting reference model for possible PV/wind hybrid energy-harvesting extensions and for consistency with the broader renewable-energy discussion. The wind model is not used in the current EBCS optimization constraints, scheduling process, or simulation results.

A. PV Energy Model Used in EBCS

PV energy harvested by each sensor node is computed as

$$E_{\text{PV}} = P_{\text{STC}} \left[1 + \beta_p (T_{\text{cell}} - T_{\text{STC}})\right] \frac{H_t}{H_{\text{STC}}} \tag{A6}$$

where T_{STC} and T_{cell} are the module cell temperatures under standard test conditions and actual operating conditions, β_p is the power temperature coefficient, and H_{STC} and H_t are the reference and actual global solar irradiance incident on the PV module surface [36], [48].

B. Supplementary Wind-Harvesting Reference Model

For a sensor node equipped with a small-scale wind-harvesting unit, the wind energy can be described by the following standard reference model:

$$E_{\text{W}} = \begin{cases} P_{\text{rat}} \dfrac{V_{Z,t} - V_{\text{cut-in}}}{V_{\text{rat}} - V_{\text{cut-in}}}, & V_{\text{cut-in}} < V_{Z,t} < V_{\text{rat}} \\ P_{\text{rat}}, & V_{\text{rat}} \le V_{Z,t} \le V_{\text{cut-off}} \\ 0, & V_{Z,t} \le V_{\text{cut-in}} \text{ or } V_{Z,t} > V_{\text{cut-off}} \end{cases} \tag{A7}$$

where P_{rat} is the rated power at rated wind speed V_{rat}, $V_{\text{cut-in}}$ and $V_{\text{cut-off}}$ are the cut-in and cutoff wind speeds, and $V_{Z,t}$ is the wind speed at turbine hub height, computed as

$$V_{Z,t} = V_{0,t} \left(\frac{h_Z}{h_0}\right)^{\alpha} \tag{A8}$$

where $V_{0,t}$ is the reference wind speed and α is the wind shear exponent [49], [50].

Additional validation and parameter guidance for small-scale wind turbines and combined PV/wind systems are provided in [59]. These wind-related expressions are included only as a supplementary reference for hybrid renewable-energy extensions and are not used in the EBCS scheduling optimization or simulation evaluation.

Appendix III
Economic and Eco-Environmental Analysis

To complement the WRSN node-level analysis, we provide an eco-environment assessment including LCOE, PBTM, and CO_2-related environmental cost frameworks. The LCOE is expressed as

$$LCOE = \frac{r(1+r)^n}{(1+r)^n - 1} \cdot C + C_{O\&M} - \frac{C_{CO2}}{E_t} \tag{A9}$$

where C is the initial investment, $C_{O\&M}$ is operation and maintenance cost, C_{CO2} represents the social cost of CO_2 emissions, and E_t is the total energy produced [55], [56].

The PBTM is defined as

$$PBTM = \frac{C}{Income} \tag{A10}$$

where *Income* is the annual energy savings or revenue [53], [57].

CO_2 environmental cost (CCO_2) is computed as

$$CCO_2 = EF_{CO2} \cdot E_t \cdot \phi_{CO2} \tag{A11}$$

where EF_{CO2} is the CO_2 emission factor (kg CO_2/kWh) and ϕ_{CO2} is the social cost of carbon (default 70/t CO_2) [46], [58].

In the context of WRSNs, these eco-environment metrics highlight the broader implications of renewable-energy integration at the sensor node level. Incorporating CCO_2 into energy allocation demonstrates how the EBCS scheduling strategy can maintain ENO while reducing environmental impacts. Scenarios with lower PV availability or shorter daylight hours increase potential CO_2 costs if nodes require additional backup, while optimized PV scheduling ensures nodes remain energy-neutral and CO_2 emissions are minimized. These results illustrate the practical link between node-level scheduling decisions and environmental sustainability in smart-city sensor networks.

References

[1] Z.-G. Chen, Y. Lin, Y.-J. Gong, Z.-H. Zhan, and J. Zhang, "Maximizing lifetime of range-adjustable wireless sensor networks: A neighborhood-based estimation of distribution algorithm," *IEEE Trans. Cybern.*, vol. 51, no. 11, pp. 5433–5446, Nov. 2021.

[2] A. Shafique, B. Cheng, B. Zhao, G. N. Alwakid, and M. I. U. Haq, "Optimized autonomous computing with trusted resilient data management for IoT emerging networks," *IEEE Sensors J.*, vol. 25, no. 11, pp. 20778–20785, Jun. 2025.

[3] V. F. Adanvo, S. Mafra, S. Montejo-Sánchez, F. A. Tondo, and R. D. Souza, "Analytical modeling of slotted Aloha-based direct-to-satellite-IoT sensor networks over Nakagami-m fading channels," *IEEE Sensors J.*, vol. 26, no. 2, pp. 3264–3277, Jan. 2026, http://dx doi: doi.org/10.1109/JSEN.2025.3635197.

[4] Z. Liu, G. Jiang, Y. Wu, T. Wang, S. Liu, and Z. Ouyang, "K-coverage estimation for irregular targets in wireless visual sensor networks deployed in complex region of interest," *IEEE Sensors J.*, vol. 25, no. 10, pp. 18370–18383, May 2025.

[5] C. Zhang, Y. Li, P. Xu, C.-Y. Chang, and D. S. Roy, "Dynamic probabilistic sensing for enhanced target coverage in WRSNs," *IEEE Sensors J.*, vol. 24, no. 16, pp. 26699–26713, Aug. 2024.

[6] P. Xu, Y. Li, C.-Y. Chang, C.-H. Kuo, and D. S. Roy, "Dynamic weather-adaptive enhanced barrier coverage with adjustable-range sensors for WRSNs," *J. Internet Technol.*, vol. 26, no. 4, pp. 523–538, Jul. 2025.

[7] S. Sarang, G. M. Stojanović, M. Drieberg, S. Stankovski, K. Bingi, and V. Jeoti, "Machine learning prediction based adaptive duty cycle MAC protocol for solar energy harvesting wireless sensor networks," *IEEE Access*, vol. 11, pp. 17536–17552, 2023.

[8] M. Abdel-Basset, H. Hawash, R. K. Chakrabortty, and M. Ryan, "Energy-Net: A deep learning approach for smart energy management in IoT-based smart cities," *IEEE Internet Things J.*, vol. 8, no. 15, pp. 12422–12437, Aug. 2021.

[9] D. K. Sah, A. Hazra, N. Mazumdar, A. C. S. Rao, and T. Amgoth, "An efficient scheduling approach for target coverage in solar powered Internet of Things," *IEEE Trans. Sustain. Comput.*, vol. 10, no. 5, pp. 1043–1055, Sep. 2025.

[10] X. Zhu and M. Zhou, "Lifetime-guaranteed cost-minimized heterogeneous visual sensor networks with feature collection for effective target coverage in 3-D space," *IEEE Sensors J.*, vol. 26, no. 3, pp. 5106–5114, Feb. 2026, http://dx doi: .doi.org/10.1109/JSEN.2025.3635175.

[11] J. Ye, Y. Xiong, H. Dong, A. Yu, and J. She, "A low-cost enhanced heterogeneous barrier construction method for multitarget intrusion monitoring," *IEEE Sensors J.*, vol. 25, no. 13, pp. 25925–25937, Jul. 2025.

[12] C.-F. Cheng and W.-H. Lin, "Deterministic target-barrier coverage with importance-aware sensor deployment in IIoT," *IEEE Sensors J.*, vol. 25, no. 19, pp. 37370–37382, Oct. 2025.

[13] P. An, P. Yang, X. Cao, C. You, Q. S. T. Quek, and D. O. Wu, "Channel estimation refinement for tethered aerial platform enabled multi-user communication systems," in *Proc. IEEE/CIC Int. Conf. Commun. China (ICCC)*, Aug. 2024, pp. 2137–2142.

[14] Q. Zhang, C.-Y. Chang, Z. Dong, and D. S. Roy, "TCSAR: Target coverage mechanism for sensors with adjustable sensing range in WRSNs," *IEEE Sensors J.*, vol. 22, no. 4, pp. 3756–3765, Feb. 2022.

[15] P. Wang, Y. Xiong, J. She, and A. Yu, "Optimization method for node deployment of closed-barrier coverage in hybrid directional sensor networks," *IEEE Sensors J.*, vol. 24, no. 9, pp. 15421–15433, May 2024.

[16] P. Manna, S. Majumder, and N. H. Singh, "A hybrid optimization strategy for k-coverage maximization in wireless sensor and IoT networks," in *Proc. 3rd Int. Conf. Intell. Syst., Adv. Comput. Commun. (ISACC)*, Feb. 2025, pp. 659–665.

[17] J. Chang, X. Shen, W. Bai, and X. Li, "Energy-efficient barrier coverage based on nodes alliance for intrusion detection in underwater sensor networks," *IEEE Sensors J.*, vol. 22, no. 4, pp. 3766–3776, Feb. 2022.

[18] W. Xu, W. Liang, X. Jia, H. Kan, Y. Xu, and X. Zhang, "Minimizing the maximum charging delay of multiple mobile chargers under the multi-node energy charging scheme," *IEEE Trans. Mobile Comput.*, vol. 20, no. 5, pp. 1846–1861, May 2021.

[19] C. Shang, C.-Y. Chang, W.-H. Liao, and D. S. Roy, "RLR: Joint reinforcement learning and attraction reward for mobile charger in wireless rechargeable sensor networks," *IEEE Internet Things J.*, vol. 10, no. 18, pp. 16107–16120, Sep. 2023.

[20] P. Xu, J. Wu, C.-Y. Chang, C. Shang, and D. S. Roy, "MCDP: Maximizing cooperative detection probability for barrier coverage in rechargeable wireless sensor networks," *IEEE Sensors J.*, vol. 21, no. 5, pp. 7080–7092, Mar. 2021.

[21] S. J. Lee, F. Safdarian, and T. J. Overbye, "Validation of wind and PV power generation using historical and forecast weather data," in *Proc. IEEE Texas Power Energy Conf. (TPEC)*, Feb. 2025, pp. 1–6.

[22] A. B. Kathole, D. Jadhav, K. N. Vhatkar, S. Amol, and N. Gandhewar, "Solar energy prediction in IoT system based optimized complex-valued spatio-temporal graph convolutional neural network," *Knowl.-Based Syst.*, vol. 304, Nov. 2024, Art. no. 112400.

[23] H. P. Gupta, S. V. Rao, and T. Venkatesh, "Sleep scheduling protocol for k-coverage of three-dimensional heterogeneous WSNs," *IEEE Trans. Veh. Technol.*, vol. 65, no. 10, pp. 8423–8431, Oct. 2016.

[24] A. Rossi, A. Singh, and M. Sevaux, "An exact approach for maximizing the lifetime of sensor networks with adjustable sensing ranges," *Comput. Oper. Res.*, vol. 39, no. 12, pp. 3166–3176, Dec. 2012.

[25] Q. Li, N. Zhang, M. Cheffena, and X. Shen, "Channel-based optimal back-off delay control in delay-constrained industrial WSNs," *IEEE Trans. Wireless Commun.*, vol. 19, no. 1, pp. 696–711, Jan. 2020.

[26] C. Wang, J. Li, F. Ye, and Y. Yang, "A mobile data gathering framework for wireless rechargeable sensor networks with vehicle movement costs and capacity constraints," *IEEE Trans. Comput.*, vol. 65, no. 8, pp. 2411–2427, Aug. 2016.

[27] Q. Yu, C. Yang, G. Dai, L. Peng, and J. Li, "A novel penalty function-based interval constrained multi-objective optimization algorithm for uncertain problems," *Swarm Evol. Comput.*, vol. 88, Jul. 2024, Art. no. 101584.

[28] M. H. Zafar, S. K. R. Moosavi, and F. Sanfilippo, "Neuromorphic event camera-based object recognition and grasping position detection using a transfer learning-enhanced multi-task model," *IEEE Trans. Autom. Sci. Eng.*, vol. 22, pp. 20169–20181, 2025.

[29] D. A. Guimarães, E. P. Frigieri, and L. J. Sakai, "Influence of node mobility, recharge, and path loss on the optimized lifetime of wireless rechargeable sensor networks," *Ad Hoc Netw.*, vol. 97, Feb. 2020, Art. no. 102025.

[30] S. M. J. Jalali, S. Ahmadian, A. Kavousi-Fard, A. Khosravi, and S. Nahavandi, "Automated deep CNN-LSTM architecture design for solar irradiance forecasting," *IEEE Trans. Syst., Man, Cybern., Syst.*, vol. 52, no. 1, pp. 54–65, Jan. 2022.

[31] W.-Y. Chang, P. Soma, H. Chen, H. Chang, and C.-W. Tsai, "A hybrid firefly with dynamic multi-swarm particle swarm optimization for WSN deployment," *J. Internet Technol.*, vol. 24, no. 4, pp. 825–832, 2023.

[32] Y. Kan, C.-Y. Chang, S.-J. Wu, C.-H. Kuo, and D. S. Roy, "CSCP: Energy charging mechanism for surveillance quality, network connectivity and perpetual lifetime in WRSNs," *J. Internet Technol.*, vol. 24, no. 2, pp. 461–468, 2023.

[33] W. Wen, C.-Y. Chang, Q. Zhang, and D. S. Roy, "PLPR: Joint perpetual lifetime and path reduction for energy recharging using multiple mobile chargers in WRSNs," *IEEE Sensors J.*, vol. 24, no. 19, pp. 31157–31164, Oct. 2024.

[34] Y. Nassar et al., "Towards green economy: Case of electricity generation sector in Libya," *Sol. Energy Sustain. Develop. J.*, vol. 14, no. 1, pp. 334–360, Apr. 2025.

[35] Y. F. Nassar et al., "Technical and environmental cost-benefit analysis of strategies towards a green economy in the electricity sector in Libya," *Econ. POLICY ENERGY Environ.*, no. 2, pp. 133–167, Nov. 2025.

[36] A. Alkhazmi et al., "Design and analysis of PV solar street lighting systems in remote areas: A case study," *Wadi Alshatti Univ. J. Pure Appl. Sci.*, vol. 4, no. 1, pp. 1–14, Dec. 2025.

[37] Y. F. Nassar, H. J. El-Khozondar, and M. A. Fakher, "The role of hybrid renewable energy systems in covering power shortages in public electricity grid: An economic, environmental and technical optimization analysis," *J. Energy Storage*, vol. 108, Feb. 2025, Art. no. 115224.

[38] M. Khaleel, Z. Yusupov, N. Yasser, and H. J. El-Khozondar, "Enhancing microgrid performance through hybrid energy storage system integration: ANFIS and GA approaches," *Int. J. Electr. Eng. Sustainability*, vol. 1, no. 2, pp. 38–48, Jun. 2023.

[39] M. Khaleel, Z. Yusupov, B. Alfalh, M. T. Guneser, Y. Nassar, and H. El-Khozondar, "Impact of smart grid technologies on sustainable urban development," *Int. J. Electr. Eng. Sustainability*, vol. 2, no. 2, pp. 62–82, Jun. 2024.

[40] H. J. El-Khozondar, R. J. El-Khozondar, Y. F. Nassar, and F. El-Batta, "Technical-economical-environmental assessment of grid-connected hybrid renewable energy power system for Gaza strip-palestine," *Eng. Sci. Technol., Int. J.*, vol. 69, Sep. 2025, Art. no. 102120.

[41] B. Ahmed, Y. Nassar, H. El-Khozondar, and M. Khaleel, "Optimal design of hybrid renewable energy system (PV/wind/PHS) under multiple constraints of connection to the electricity grid: A case study," *Wadi Alshatti Univ. J. Pure Appl. Sci.*, vol. 4, no. 1, pp. 83–93, Jan. 2026.

[42] A. A. Ahmed, Y. F. Nassar, N. M. Abdulla, and A. M. Bashir, "AI-powered energy forecasting: ANext-gen approach for smart grids and sustainable power systems," *Eurasian J. Theor. Appl. Sci.*, vol. 1, no. 2, pp. 1–15, Apr. 2025.

[43] A. Abduallah et al., "Leveraging hydrogen for covering energy shortage in an electricity subgrid," *Wadi Alshatti Univ. J. Pure Appl. Sci.*, vol. 4, no. 1, pp. 245–254, Mar. 2026.

[44] H. J. El-Khozondar, F. El-Batta, R. J. El-Khozondar, Y. Nassar, M. Alramlawi, and S. Alsadi, "Standalone hybrid PV/wind/diesel-electric generator system for a COVID-19 quarantine center," *Environ. Prog. Sustain. Energy*, vol. 42, no. 3, May 2023, Art. no. e14049.

[45] H. El-Khozondar and F. El-Batta, "Solar energy as an alternative to conventional energy in Gaza strip: Questionnaire based study," *An-Najah Univ. J. Res. - A, Natural Sci.*, vol. 32, no. 1, pp. 47–74, Feb. 2018.

[46] M. Elnaggar, H. J. El-Khozondar, M. J. K. Bashir, and W. A. Salah, "Enhancing solar water heater system for utmost useful energy gain and reduction in greenhouse gas emissions in Gaza," *Int. J. Environ. Sci. Technol.*, vol. 20, no. 4, pp. 3749–3764, Apr. 2023.

[47] H. Al-Najjar, C. Pfeifer, R. Al Afif, and H. J. El-Khozondar, "Performance evaluation of a hybrid grid-connected photovoltaic biogas-generator power system," *Energies*, vol. 15, no. 9, p. 3151, Apr. 2022.

[48] H. J. El-Khozondar et al., "Sustainable street lighting in Gaza: Solar energy solutions for main street," *Energy* vol. 360, vol. 4, Dec. 2025, Art. no. 100042.

[49] H. Al-Najjar, H. J. El-Khozondar, C. Pfeifer, and R. Al Afif, "Hybrid grid-tie electrification analysis of bio-shared renewable energy systems for domestic application," *Sustain. Cities Soc.*, vol. 77, Feb. 2022, Art. no. 103538.

[50] M. Elnaggar et al., "Sustainable energy, economic, and environmental impacts of small-scale wind turbines: A comprehensive study," *Int. J. Energy Res.*, vol. 46, no. 8, pp. 10808–10821, Jun. 2022.

[51] H. J. El-Khozenadar, T. Khatib, B. Attaee, and R. J. El-Khozondar, "Assessment of solar e-cookers social acceptance in Gaza strip," *Sci. Rep.*, vol. 12, no. 1, Oct. 2022, Art. no. 17226.

[52] H. El-Khozondar, R. El-Khozondar, W. Shbair, and A. Eljamassi, "Social awareness of the use of renewable energy among the students of the faculty of engineering, Islamic University, Gaza, Palestine," *An-Najah Univ. J. Res. - B, Humanities*, vol. 36, no. 6, pp. 1173–1194, Jun. 2022.

[53] Y. F. Nassar et al., "Estimation of CO_2 emission within Libya's electricity generation sector," *Next Res.*, vol. 2, no. 3, Sep. 2025, Art. no. 100567.

[54] S. M. Ahmad, A. Agrira, and Y. F. Nassar, "The impact of loss of power supply probability on design and performance of wind/pumped hydropower energy storage hybrid system," *Wadi Alshatti Univ. J. Pure Appl. Sci.*, vol. 3, no. 2, pp. 52–62.

[55] A. A. Amhimmid, W. A. El-Osta, Y. F. Nassar, H. J. El-Khozondar, and M. A. Salem, "Financial modeling of social and environmental impacts of wind farm in urban zones: A case study of Zawia–Libya," *Int. J. Energy Environ. Eng.*, vol. 15, no. 4, pp. 1–20, Dec. 2024.

[56] M. Abdunnabi, N. Etiab, Y. F. Nassar, H. J. El-Khozondar, and R. Khargotra, "Energy savings strategy for the residential sector in Libya and its impacts on the global environment and the nation economy," *Adv. Building Energy Res.*, vol. 17, no. 4, pp. 379–411, May 2023.

[57] H. El-Khozondar et al., "Economic and environmental implications of solar energy street lighting in urban regions: A case study," *Wadi Alshatti Univ. J. Pure Appl. Sci.*, vol. 3, no. 1, pp. 142–151, Mar. 2025.

[58] M. Khaleel, I. Imbayah, Y. Nassar, and H. J. El-Khozondar, "Renewable energy transition pathways and net-zero strategies," *Int. J. Electr. Eng. Sustainability*, vol. 3, no. 4, pp. 1–16, Dec. 2025.

[59] M. Elnaggar, W. A. Salah, H. J. El-Khozondar, Y. F. Nassar, and M. J. K. Bashir, "Leveraging wind energy for electricity and hydrogen production: A sustainable solution to power shortages and eco-friendly alternative fuel," *Adv. Energy Sustainability Res.*, vol. 7, no. 2, Feb. 2026, Art. no. e202500049.

Pei Xu (Member, IEEE) received the Ph.D. degree in computer science and technology from Anhui University, Hefei, China, in 2020.

He is currently a Lecturer with the School of Artificial Intelligence and Big Data, Hefei University, Hefei. His current research interests include smart sensing technology, the Internet of Things, and deep learning.

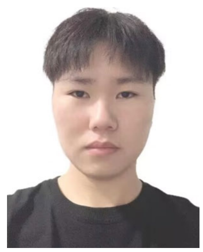

Shi-Long Han received the B.S. degree in software engineering from Bengbu University, Bengbu, China, in 2022. He is currently pursuing the M.S. degree with the School of Artificial Intelligence and Big Data, Hefei University, Hefei, China.

His research interests include wireless sensor networks, the Internet of Things (IoT), and optimization theory.

Chih-Yung Chang (Member, IEEE) received the Ph.D. degree in computer science and information engineering from National Central University, Taoyuan, Taiwan, in 1995.

He is currently a Distinguished Professor with the Department of Computer Science and Information Engineering and the Department of Artificial Intelligence, Tamkang University, New Taipei, Taiwan. His current research interests include artificial intelligence, deep learning and machine learning, the Internet of Things, and wireless sensor networks.

Dr. Chang is the Co-Chair of ACM SIGMOBILE, Taiwan. He has been serving as an Associate Guest Editor for several SCI-indexed journals, including *International Journal of Ad Hoc and Ubiquitous Computing* since 2011, *Journal of Applied Science and Engineering* since 2018, *International Journal of Distributed Sensor Networks* from 2012 to 2014, *IET Communications* in 2011, *Telecommunication Systems* in 2010, *Journal of Information Science and Engineering* in 2008, and *Journal of Internet Technology* from 2004 to 2008.

Diptendu Sinha Roy (Senior Member, IEEE) received the Ph.D. degree in engineering from the Birla Institute of Technology, Mesra, India, in 2010.

He was with the Department of Computer Science and Engineering, National Institute of Science and Technology, Berhampur, India. In 2016, he joined the Department of Computer Science and Engineering, National Institute of Technology (NIT) Meghalaya, Shillong, India, as an Associate Professor, where he has been the Chair of the Department of Computer Science and Engineering since January 2017. His current research interests include software reliability, distributed and cloud computing, and the Internet of Things (IoT), specifically applications of artificial intelligence/machine learning for smart integrated systems.

Dr. Roy is a member of the IEEE Computer Society.